

RESEARCH ARTICLE

WILEY

Large-eddy simulation of subsonic turbulent jets using the compressible lattice Boltzmann method

Khalid Noah^{1,2}  | Fue-Sang Lien¹ | Eugene Yee¹

¹Department of Mechanical and Mechatronics Engineering, University of Waterloo, Waterloo, Ontario, Canada

²Department of Mechanical Engineering, University of Tobruk, Tobruk, Libya

Correspondence

Khalid Noah, Department of Mechanical and Mechatronics Engineering, University of Waterloo, Waterloo, ON N2L 3G1, Canada.

Email: knoah@uwaterloo.ca

Funding information

Canadian Bureau for International Education, Grant/Award Number: 2755

Summary

The lattice Boltzmann method (LBM) is a powerful technique for the computational modeling of a wide variety of single-s and multiphase flows involving complex geometries. Although the LBM has been demonstrated to be effective for the solution of incompressible flow problems, there are limitations when this methodology is applied to the solution of compressible flows, especially for flows at high Mach numbers. In this article, we investigate strategies to overcome some of the limitations associated with the application of LBM to compressible flows. To this purpose, one of the key contributions of this study is the synthesis and integration of previous efforts concerning the formulation of LBM for the large-eddy simulation (LES) of compressible turbulent flows in the subsonic flow regime. It is shown how certain limitations of applying the LBM to compressible flows can be addressed by using either a higher order Taylor series expansion of the Maxwell–Boltzmann equilibrium distribution function or using the Kataoka and Tsutahara (KT) LBM model formulation for compressible flows. The proposed LBM/LES methodology for compressible flows has been combined with the Kirchhoff integral formulation for computational aeroacoustics and used to simulate the flow and acoustic fields of compressible jet flows at high subsonic speeds with practical relevance for providing a better understanding of problems associated with jet noise. In this context, simulations of the physics associated with the jet flow and concomitant noise in the near- and far-field regimes were conducted using the proposed framework of a compressible LBM/LES and Kirchhoff integral method. The results of the subsonic isothermal and nonisothermal jet flow simulations for the flow and acoustic fields have been compared with available numerical and experimental results with generally good to excellent agreement.

KEYWORDS

compressible lattice Boltzmann method, higher order equilibrium distribution function, jet noise prediction, Kataoka and Tsutahara model, large-eddy simulation

1 | INTRODUCTION

There are two methodologies that have been used to address various computational fluid mechanics problems; namely, applying either a macroscopic or a microscopic model. Interestingly, there is an intermediate or

mesoscopic approach that has attracted the interest of researchers in computational fluid mechanics. This mesoscopic approach utilizes the lattice Boltzmann equation for the simulation of computational fluid dynamics problems and provides a logical bridge between the microscopic and macroscopic approaches.¹ The first step required for the solution of the Navier–Stokes or Euler equation in the continuum (macroscopic) approximation to fluid flow is to discretize the equation using a finite volume, a finite element, or a finite difference method. A macroscopic approach for fluid flow simulation is effective for addressing numerous applications. However, for applications involving complex geometries, it can be challenging to apply boundary conditions within the context of a macroscopic approach.²

Over the past two decades, the lattice Boltzmann method (LBM) has emerged as a competitive scheme for simulating various complex fluid systems owing to the ease of applying boundary conditions in these systems.³ More specifically, the physical insight in the application of these boundary conditions is clearer and their implementation is more straightforward in the LBM in comparison with the more conventional computational fluid dynamics (CFD). Furthermore, complex and coupled flow problems can be readily implemented in a massively parallel computing environment⁴ using the LBM when an explicit time-stepping scheme is employed. Finally, the LBM has been demonstrated to be effective for the solution of various incompressible flow problems.

In spite of these advantages, it is important to note that the application of the LBM to the simulation of compressible turbulent flows, particularly at high Mach number involving shock waves, is still at an early stage of development. In consequence, a great deal of attention in the development of the LBM has been focused recently on its application to the solution of compressible turbulent flows.⁵ To date, LBM has been used as a direct numerical simulation (DNS) method for the simulation of relatively low-Reynolds number flows.⁶ However, the LBM can be combined with large-eddy simulation (LES) to provide predictions of instantaneous flow characteristics and large turbulent flow structures, in contrast to the traditional Reynolds-averaged Navier–Stokes (RANS) approach which provides only time-averaged flow quantities.⁷

In recent years, researchers have proposed various strategies for combining the LBM with LES for the simulation of turbulent flows. Fernandino et al.⁸ incorporated the Smagorinsky subgrid scale (SGS) model into the LBM for the simulation of a free surface flow in a wide rectangular duct. While discrepancies were evident in the mean flow structures due to the use of a coarse grid close to the wall, the results in the study nevertheless showed that a good qualitative agreement between the experimental data and the predictions can be obtained using the proposed methodology. Dong et al.⁹ incorporated an inertial-range-consistent Smagorinsky model in the LBM (used in conjunction with a D3Q19 lattice model) as a means of assessing the effectiveness of the LBM–LES technique for the simulation of an isotropic turbulent flow at low Mach numbers. Dong and Sagaut¹⁰ incorporated a number of different SGS models within the LBM and investigated their effects on the prediction of temporal correlations in isotropic turbulence. Overall, their findings revealed that the LBM–LES model generally yielded results that were in good agreement with the experimental outcomes as well as with other numerical studies for low-Reynolds-number flows.

Chen⁵ developed a novel and simple LBM–LES for the simulation of two-dimensional turbulent flows which involved the utilization of the vorticity stream function equations (rather than the Navier–Stokes equations) for the simulation of the flows. Encouraging results were reported in this study using this approach. Si and Shi¹¹ demonstrated that LBM–LES can be used to simulate fluid flow at high Reynolds numbers. These investigators presented a detailed quantitative comparison of the predictions for the vortex position for a turbulent flow inside a cavity with experimental data. In spite of this success, the limited ability of conventional LBM for the simulation of compressible flows, especially at Mach numbers larger than 0.1, has been well documented.¹²

Buick et al.¹³ investigated the utility of incorporating the Bhatnagar, Gross, and Krook (BGK)¹⁴ collision model in an LBM for the simulation of sound waves at small density variations. Lew et al.¹⁵ applied a commercial LBM code (PowerFLOW) to predict the near-field and far-field jet noise at a Mach number of 0.4. These investigators showed that the prediction of the near-field flow statistics was in agreement with some experimental results. In addition, it was found that the predicted behavior of the sound waves was also in good agreement with some analytic expressions. Yu and Girimaji¹⁶ employed a multiple relaxation time (MRT) LBM to predict the near-field noise for a rectangular jet flow at a low Mach number of about 0.17. This study showed that the MRT-LBM can potentially provide a practical computational methodology for the LES of turbulence at a high Reynolds number.

1.1 | Contributions and perspectives of this work

In this work, we combine LES with a *compressible* LBM for the first time (to the best of the authors' knowledge) and apply this hybrid methodology to simulate compressible turbulent subsonic flows. To date, LBM has been used only in the context of a direct numerical simulation for predicting fluid flows at low-Reynolds number or combined with LES to predict *incompressible* (or, weakly compressible) turbulent flows at high-Reynolds number. This work takes on an applied perspective of formulating a methodology that can be used for the simulation of compressible turbulent flow at subsonic (and potentially transonic and supersonic) Mach numbers, with the specific goal of simulating subsonic turbulent jet flow. This hybrid LBM–LES approach for the simulation of subsonic turbulent flows, which is based on the discrete Boltzmann equation and transparent streaming and collision operations, is simpler to implement than conventional computational fluid dynamics methods and is amenable to high-performance computation on parallel computational architectures.

Given the current state-of-the-art in the application of the LBM for the simulation of compressible flows, the principal objectives of this article are: (1) to generalize and extend the LBM–LES methodology for the simulation of subsonic flow regimes for a compressible and turbulent-free jet and (2) to conduct simulations of this class of flows in order to investigate the physics of the near-field and far-field jet noise of a turbulent subsonic jet. To achieve the latter objective, the LBM–LES framework is integrated tightly with the Kirchhoff–Helmholtz integral methodology for computational aeroacoustics (owing to the fact that LBM is not appropriate for predicting directly long-range propagation of sound). This hybrid approach allows radiation sound from jet source flow to be determined (predicted) in both the near and far fields. The methods in this article are illustrated and validated on two examples of isothermal and nonisothermal subsonic turbulent jet flow that are relevant to fluid mechanics.

2 | LATTICE BOLTZMANN METHOD

The LBM evolved from the development of lattice gas automata (LGA) for the simulation of fluid flows.¹⁷ The LBM can be used to solve the nonlinear partial differential equations of fluid flow and is quite distinct from the more traditional continuum (CFD) approach for fluid flow simulation. The motivation for the development of the Boltzmann equation lies in a desire to deduce the macroscopic behavior of a fluid based on its microscopic properties.¹²

In the absence of external forces, the Boltzmann equation in a continuous position-velocity space assumes the following form:

$$\frac{\partial f}{\partial t} + \vec{v} \cdot \nabla f = \Omega, \quad (1)$$

where f is the particle distribution function defined on a phase (position-velocity) space, \vec{v} is the microscopic velocity, t is time, and Ω is the collision integral involving a complex integrodifferential expression (in general). The most complicated term in the Boltzmann equation is the collision term Ω . In 1954, Bhatnagar, Gross, and Krook (BGK)¹⁴ proposed a simplification of the collision integral operator in order to facilitate the solution of the Boltzmann equation. The BGK model is based on the assumption that the net effect of particle collisions causes the particle distribution function f to relax toward a local equilibrium particle distribution f^{eq} with a certain characteristic time. The BGK closure model for the nonlinear integral collision operator assumes the following form:

$$\Omega = -\omega(f - f^{eq}) = -\frac{1}{\tau}(f - f^{eq}), \quad (2)$$

where $\omega \equiv 1/\tau$ is the collision frequency (or, equivalently, τ is the collision relaxation time), and f^{eq} is the local equilibrium distribution function.

Substituting Equation (2) into Equation (1) results in the following simplified form of the Boltzmann equation:

$$\frac{\partial f}{\partial t} + \vec{v} \cdot \nabla f = -\frac{1}{\tau}(f - f^{eq}). \quad (3)$$

With the specification of a discrete velocity set \vec{c}_i ($i = 0, 1, \dots, Q-1$) for Q directions, the Boltzmann equation with the BGK approximation for the collision integral can be discretized as

$$\frac{\partial f_i}{\partial t} + \vec{c}_i \cdot \nabla f_i = -\frac{1}{\tau}(f_i - f_i^{eq}), \quad (4)$$

where f_i and f_i^{eq} are the discrete particle and equilibrium distributions associated with the i th discretized velocity direction. Further discretizing this equation in time and space gives the lattice Boltzmann equation (LBE)

$$f_i(\vec{x} + \vec{c}_i \Delta t, t + \Delta t) - f_i(\vec{x}, t) = -\frac{\Delta t}{\tau} (f_i(\vec{x}, t) - f_i^{eq}(\vec{x}, t)), \quad i = 0, 1, \dots, Q-1, \quad (5)$$

where Δt is the size of the time step taken along the characteristic line defined by \vec{c}_i . The left-hand-side of the LBE corresponds to the so-called streaming step in which f_i is streamed along \vec{c}_i in the time step Δt . The right-hand-side of the LBE is the so-called collision step in which the discrete particle distribution f_i relaxes toward the local equilibrium distribution f_i^{eq} on a time scale determined by the collision relaxation time τ .

The local equilibrium distribution function f^{eq} assumes the following Maxwell–Boltzmann form in a D -dimensional space:

$$f^{eq} = \frac{\rho}{(2\pi RT)^{D/2}} \exp\left(-\frac{(\vec{v} - \vec{u})^2}{2RT}\right), \quad (6)$$

where the equilibrium distribution is expressed in terms of the macroscopic fluid properties of (constant) density ρ , velocity \vec{u} , and temperature T as well as the gas constant R . The discrete equilibrium distribution f_i^{eq} can be derived from an expansion of the Maxwell–Boltzmann distribution function f^{eq} in terms of Hermite polynomials. Using the Gauss–Hermite quadrature, the following discrete equilibrium distribution f_i^{eq} can be obtained for an incompressible (very low Mach number) flow:

$$f_i^{eq}(x, t) = w_i \rho \left(1 + \frac{\vec{c}_i \cdot \vec{u}}{c_s^2} + \frac{(c_i \cdot \vec{u})^2}{2c_s^4} - \frac{\vec{u}^2}{2c_s^2} \right) + O(\vec{u}^3), \quad (7)$$

where $c_s = |\vec{c}_i| / \sqrt{3}$ is the speed of sound. Furthermore, w_i are the weighting coefficients satisfying

$$\sum_{i=0}^{Q-1} w_i = 1, \quad (8)$$

where Q is the total number of discrete particle velocities. These weighting coefficient are determined by the specific discrete velocity set which is dependent on the lattice model (e.g., for the D2Q9 discrete velocity set where $D=2$ and $Q=9$, the weighting coefficients are $w_i = 4/9$ for $i=0$, $w_i = 1/9$ for $i=1, \dots, 4$ and $w_i = 1/36$ for $i=5, \dots, 8$).

3 | COMPRESSIBLE LATTICE BOLTZMANN METHOD

The low-Mach-number limitation for the conventional LBE described previously arises from the use of a truncated expansion (typically accurate up to second order only) of the Maxwell–Boltzmann equilibrium distribution function, as summarized in Equation (7). This simplification stems from the need to facilitate the integration of the Boltzmann equation in a discrete velocity space using the Gauss–Hermite quadrature. However, the higher order truncated terms in the Taylor series expansion of the Maxwell–Boltzmann equilibrium distribution function f_i^{eq} become significant when the Mach number increases.

The literature includes reports of a number of strategies that have been developed for overcoming the low-Mach-number limitation and providing an LBM that is appropriate for the simulation of a compressible flow at higher Mach numbers. This involves constructing a better approximation for the equilibrium distribution function f^{eq} to use in place of the severely truncated approximation of f_i^{eq} given in Equation (7). The higher order terms in the expansion of the equilibrium distribution become significant at higher Mach numbers. To generalize the LBM for the simulation of compressible flow at higher Mach numbers, researchers have focused on two strategies: namely (1) formulating higher order expansions of the Maxwell–Boltzmann equilibrium distribution and (2) finding alternative forms for the equilibrium distribution (different than the Maxwell–Boltzmann form) which exhibit smaller truncation errors for the simulation of flows at a higher Mach number.

A number of investigations has reported several important advances with respect to the application of LBM for the simulation of compressible flows. Shouxin et al.¹⁸ introduced a new model for the equilibrium distribution function involving three energy levels. Their two-dimensional (2D) model requires 13 or 17 lattice velocities. Shan and He¹⁹ presented a new model for use with a compressible LBM based on a third-order expansion of the equilibrium distribution function. The Gauss–Hermite quadrature was used to approximate the relevant integrals that define the hydrodynamic moments, allowing the identification of the weight coefficients w_i in the expansion. Yan et al.²⁰ proposed a set of new weighting coefficients in their discretization of the equilibrium distribution function in the context of the D2Q9 lattice model that they suggest is appropriate for the LBM simulation of inviscid compressible flows at high Mach numbers.

Kataoka and Tsutahara^{21,22} introduced two compressible LBM models to solve the Euler and Navier–Stokes equations. They found that the specific heat ratio cannot be chosen freely, so they developed a new equilibrium distribution function to overcome this deficiency. Qu et al.²³ proposed a new method involving the adoption of a circular equilibrium distribution function for use in an LBM for the simulation of an inviscid compressible flow at a high Mach number. The circular function is a probability distribution function defined on a unit circle. This form of the equilibrium distribution not only simplifies the integration of hydrodynamic moments in the particle velocity space but also, more importantly, is applicable to the solution of the Navier–Stokes equation.

Wang et al.²⁴ proposed an implicit–explicit finite-difference Runge–Kutta scheme for the numerical solution of the discrete Boltzmann equation (traditionally addressed using a streaming–collision procedure) and applied the scheme to simulate compressible flows. Li et al.²⁵ developed two related approaches to model compressible flows based on an LBM that utilized a coupled double-distribution function in conjunction with a multispeed lattice that can accommodate arbitrary values of the specific heat ratio and Prandtl number. A fully three-dimensional (3D) nonfree parameter LBM for inviscid compressible flows was proposed by Li et al.²⁶ in which they replaced the Maxwellian equilibrium distribution used in standard LBM with a 3D generalization of the circle function (proposed earlier by Qu et al.²³) which is approximated on the lattice using a 3D Lagrangian interpolation polynomial. Finally, Wang et al.²⁷ proposed a polynomial function approach for modeling the equilibrium and energy distribution functions (coupled using an equation of state) and applied this approach to simulate viscous compressible flows.

The objective in this article is to utilize a model for a compressible LBM schema in order to conduct a large-eddy simulation (LES) of the flow in a *turbulent* jet at high subsonic speeds in three dimensions. Toward this objective, we select two different approaches for modeling compressible flow using an LBM schema and then show how these schema can be incorporated within an LES framework and used to simulate turbulent compressible flow and, more specifically, turbulent jet flow at subsonic Mach number. Within this context, the two different approaches that have been investigated in this study are those proposed by Shan and He¹⁹ which utilizes a higher order expansion of the Maxwell–Boltzmann equilibrium distribution function and by Kataoka and Tsutahara^{21,22} who used an alternative (different) functional form for the equilibrium distribution function.

3.1 | Higher order equilibrium distribution function

A second-order approximation of the Maxwell–Boltzmann equilibrium distribution (cf. Equation (6)) is usually used in conjunction with a conventional LBM for the simulation of an incompressible flow. Shan and He¹⁹ generalized this basic approach by using a third-order expansion of the equilibrium distribution for simulation of low-Mach-number flows. To relax the compressibility limitations of the conventional LBM, these investigators also used sixth-order Hermite polynomials in the representation of the Maxwell–Boltzmann equilibrium distribution. The form of the equilibrium distribution for this approximation is given by

$$\begin{aligned}
 f_i^{eq} = w_i \rho \bigg\{ & 1 + c_{i\alpha} \cdot u_\alpha + \frac{1}{2} [(c_{i\alpha} \cdot u_\alpha)^2 - u_\alpha^2] \\
 & + \frac{(T-1)}{2} (c_{i\alpha}^2 - D) + \frac{c_{i\alpha} \cdot u_\alpha}{6} [(c_{i\alpha} \cdot u_\alpha)^2 - 3u_\alpha^2] \\
 & + \frac{T-1}{2} (c_{i\alpha} \cdot u_\alpha)(c_{i\alpha}^2 - D - 2) + \frac{1}{24} [(c_{i\alpha} \cdot u_\alpha)^4 - 6(c_{i\alpha} \cdot u_\alpha)^2 u_\alpha^2 + 3u_\alpha^4] \\
 & + \frac{T-1}{4} [(c_{i\alpha}^2 - D - 2)((c_{i\alpha} \cdot u_\alpha)^2 - u_\alpha^2) - 2(c_{i\alpha} \cdot u_\alpha)^2] \bigg\}
 \end{aligned} \quad (9)$$

$$\begin{aligned}
& + \frac{(T-1)^2}{8} [c_{i\alpha}^4 - 2(D+2)c_{i\alpha}^2 + D(D+2)] \\
& + \frac{u_\alpha}{120} [(c_{i\alpha} \cdot u_\alpha)^4 - 10(c_{i\alpha} \cdot u_\alpha)^2 u_\alpha^2 + 15u_\alpha^5] \\
& + \frac{T-1}{12} u_\alpha [(c_{i\alpha}^2 - D - 4)((c_{i\alpha} \cdot u_\alpha)^2 - u_\alpha^2) - 2(c_{i\alpha} \cdot u_\alpha)^2] \\
& + \frac{(T-1)^2}{8} u_\alpha [c_{i\alpha}^4 - 2(D+2)c_{i\alpha}^2 + (D+2)(D+4)] \Big\},
\end{aligned}$$

where α is an index that denotes the spatial directions in position space (Cartesian coordinates), D is the spatial dimension, T is the temperature (assumed to be nondimensionalized with respect to a reference temperature T_0), u_α is α th component of the macroscopic fluid velocity, and ρ is the macroscopic fluid density. This expansion of the equilibrium distribution was used in conjunction with the D3Q19 lattice model (see Figure 1) by Shan and He¹⁹ for the LBM simulation of compressible flows.

The macroscopic variables in Equation (9) can be determined from the moments of the discrete particle velocity distribution f_i as follows:

$$\rho = \sum_{i=0}^{Q-1} f_i, \quad (10)$$

$$\rho u_\alpha = \sum_{i=0}^{Q-1} f_i c_{i,\alpha}, \quad (11)$$

and

$$\rho \epsilon = \frac{1}{2} \sum_{i=0}^{Q-1} f_i (c_{i,\alpha} - u_\alpha)(c_{i,\alpha} - u_\alpha), \quad (12)$$

where ϵ is the internal energy. For reference, the discrete velocity set associated with the D3Q19 lattice model is given by

$$(c_{i,1}, c_{i,2}, c_{i,3}) = \begin{cases} (0, 0, 0) & i = 0; \\ (\pm 1, 0, 0), (0, \pm 1, 0), (0, 0, \pm 1) & i = 1, \dots, 6; \\ (\pm 1, \pm 1, 0), (\pm 1, 0, \pm 1), (0, \pm 1, \pm 1) & i = 7, \dots, 18. \end{cases} \quad (13)$$

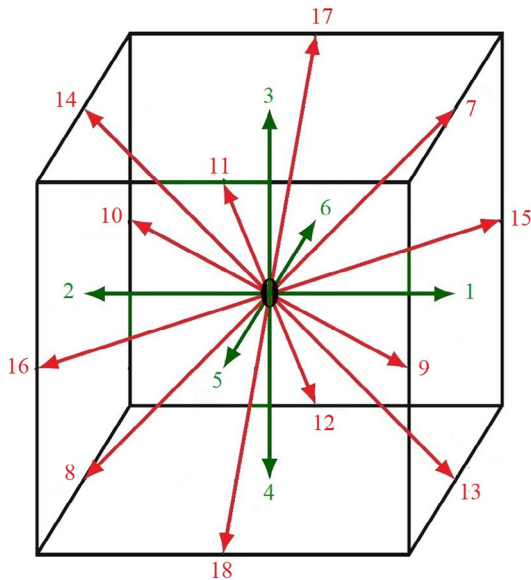
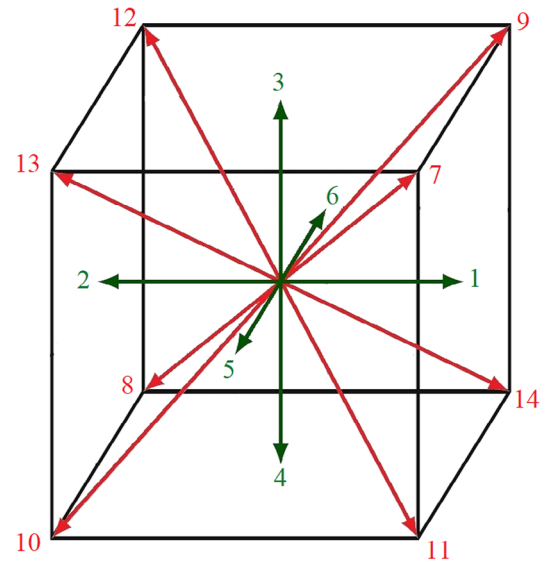


FIGURE 1 The three-dimensional (3D) D3Q19 lattice model involving a set of 19 discrete velocities [Colour figure can be viewed at wileyonlinelibrary.com]

FIGURE 2 The three-dimensional (3D) D3Q15 lattice model involving a set of 15 discrete velocities [Colour figure can be viewed at wileyonlinelibrary.com]



3.2 | Kataoka and Tsutahara models

Kataoka and Tsutahara (KT)^{21,22} developed two models for the simulation of compressible flows using the LBM. The first and second models were developed for obtaining the solutions for the compressible Navier–Stokes equation with an arbitrary specific heat ratio and for the compressible Euler equation, respectively. Both models allow the specification (prescription) of the specific heat ratio (viz., the specific heat ratio can be chosen freely in these models). To this purpose, a new variable η is introduced in order to permit the specification of the specific heat ratio at each point in the lattice structure. Furthermore, a single relaxation time (SRT) required for the definition of the BGK collision operator is prescribed as a function of the density and the temperature.

As mentioned above, one of the primary objectives of this article is to utilize the KT model in a compressible LBM schema in order to conduct a large-eddy simulation (LES) of the flow in turbulent jet at high subsonic speeds in three dimensions. Within the context of a three-dimensional simulation, it is noted that the KT model has been formulated only for the three-dimensional D3Q15 lattice by the original researchers and that it is difficult to generalize this approach to other types of lattices. In view of this, the KT LBM model was implemented using the three-dimensional D3Q15 lattice shown in Figure 2 and a subgrid-scale model was incorporated in order to model the effects of the turbulence that cannot be resolved explicitly in the simulation. This KT-LBM-LES schema will be used for the solution of the compressible Navier–Stokes equation governing the flow dynamics of a turbulent jet at subsonic speeds.

The macroscopic variables of the flow in the KT model are related to the various hydrodynamic moments of the discrete particle distribution function as follows (where in the context of the D3Q15 lattice model, $Q = 15$ in the equations below):

$$\rho = \sum_{i=0}^{Q-1} f_i, \quad (14)$$

is the macroscopic density;

$$\rho u_\alpha = \sum_{i=0}^{Q-1} f_i c_{i,\alpha}, \quad (15)$$

is the momentum density;

$$P\delta_{\alpha\beta} + \rho u_\alpha u_\beta = \sum_{i=0}^{Q-1} f_i c_{i,\alpha} c_{i,\beta}, \quad (16)$$

where P is the macroscopic pressure and $\delta_{\alpha\beta}$ is the Kronecker delta function; and

$$\rho(bRT + u_\alpha^2) = \sum_{i=0}^{Q-1} f_i(c_{i,\alpha}^2 + \eta_i^2), \quad (17)$$

where b is a prescribed constant that is related to the specific-heat ratio γ as

$$b = \frac{2}{\gamma - 1}, \quad (18)$$

with

$$\eta_i = \begin{cases} \eta_0, & i = 0; \\ 0, & i = 1, \dots, 14. \end{cases} \quad (19)$$

For reference, the discrete velocity set associated with the D3Q15 lattice model is given by

$$(c_{i,1}, c_{i,2}, c_{i,3}) = \begin{cases} (0, 0, 0) & i = 0; \\ v_1(\pm 1, 0, 0), v_1(0, \pm 1, 0), v_1(0, 0, \pm 1) & i = 1, \dots, 6; \\ \frac{v_2}{\sqrt{3}}(\pm 1, \pm 1, \pm 1) & i = 7, \dots, 14. \end{cases} \quad (20)$$

The equilibrium distribution function for the KT model is given by

$$f_i^{eq} = \rho(A_i + B_i u_\alpha c_{i,\alpha} + D_i u_\alpha c_{i,\alpha} u_\beta c_{i,\beta}), \quad i = 0, \dots, 14, \quad (21)$$

where A_i , B_i , and D_i assume the following forms:

$$A_i = \begin{cases} \frac{b-3}{\eta_0^2} T & i = 0; \\ \frac{1}{6(v_1^2 - v_2^2)} \left[-v_2^2 + \left((b-3)\frac{v_2^2}{\eta_0^2} + 3 \right) T + \frac{v_2^2}{v_1^2} u_\alpha^2 \right] & i = 1, \dots, 6; \\ \frac{1}{8(v_2^2 - v_1^2)} \left[-v_1^2 + \left((b-3)\frac{v_1^2}{\eta_0^2} + 3 \right) T + \frac{3v_1^2 - v_2^2}{2v_2^2} u_\alpha^2 \right] & i = 7, \dots, 14; \end{cases} \quad (22)$$

$$B_i = \begin{cases} 0 & i = 0; \\ \frac{-v_2^2 + (b+2)T + u_\beta^2}{2v_1^2(v_1^2 - v_2^2)} & i = 1, \dots, 6; \\ \frac{3[-v_1^2 + (b+2)T + u_\beta^2]}{8v_2^2(v_2^2 - v_1^2)} & i = 7, \dots, 14; \end{cases} \quad (23)$$

and

$$D_i = \begin{cases} 0 & i = 0; \\ \frac{1}{2v_1^4} & i = 1, \dots, 6; \\ \frac{9}{16v_2^4} & i = 7, \dots, 14. \end{cases} \quad (24)$$

The parameters appearing in Equations (19–24) are chosen to be $v_1 = 1$, $v_2 = 3$, and $\eta_0 = 2$.

4 | SUBGRID-SCALE MODELING OF TURBULENT FLOWS

The direct numerical simulation (DNS) of a fluid is based on the solution of the governing equations such as the Navier–Stokes equation, the Euler equation, or the lattice Boltzmann equation without the imposition of any additional

physical assumptions or the incorporation of subgrid-scale models. In DNS, all scales of the fluid motion are resolved explicitly in the simulation. As a consequence, the mesh grid and the time step must be chosen to be fine enough to capture the dynamics of the flow from the largest (integral) to the smallest (viscous) scales. Needless to say, DNS is prohibitively computationally expensive to conduct for high-Reynolds-number flows over a large simulation domain. Owing to this fact, an alternative is provided by large-eddy simulation (LES)²⁸ which is intermediate in incurred computational cost between DNS and turbulence closure schemes that are representative of Reynolds-averaged Navier–Stokes (RANS) approaches.

The basic idea behind LES is to compute explicitly the mean flow and the large energetic eddies, while parameterizing the small-scale flow structures that cannot be resolved by some heuristic closure model. The influence of these small-scale structures on the flow are not simulated, but their physical effects on the resolved fluid motion is parameterized using an appropriate subgrid-scale (SGS) model.²⁹ One of the most popular SGS models for accounting for the unresolved flow scales in LES is the Smagorinsky model²⁸ which is used to model the residual (fictitious) stresses arising from the application of a spatial filtering operation on the Navier–Stokes equation.⁶ In the case of the Smagorinsky SGS model, the anisotropic part of the residual stress tensor is modeled as follows:

$$\tau_{\alpha\beta} - \frac{\delta_{\alpha\beta}}{3} \tau_{\kappa\kappa} = -2\nu_t \overline{S_{\alpha\beta}} = -2C^2 \Delta^2 |\overline{S}| \overline{S_{\alpha\beta}}, \quad (25)$$

where $\delta_{\alpha\beta}$ is the Kronecker delta function, C is the Smagorinsky constant, Δ is the filter width (or grid scale), and $|\overline{S}|$ is the magnitude of the large-scale (resolved) strain-rate tensor given by

$$|\overline{S}| = (2\overline{S_{\alpha\beta}} \overline{S_{\alpha\beta}})^{1/2}, \quad (26)$$

where the resolved strain-rate tensor is defined as

$$\overline{S_{\alpha\beta}} \equiv \frac{1}{2} \left(\frac{\partial \overline{u}_\alpha}{\partial x_\beta} + \frac{\partial \overline{u}_\beta}{\partial x_\alpha} \right). \quad (27)$$

Furthermore, ν_t is the eddy viscosity of the residual fluid motion which is modeled as $\nu_t = C^2 \Delta^2 |\overline{S}|$.

The application of an LBM–LES approach for the simulation of compressible turbulent flows involves using either a higher order approximation for the equilibrium distribution function or the KT model as described previously. To proceed further, we need to specify the (effective) relaxation time τ . The basic strategy underpinning the incorporation of LES in the LBM framework is to formulate an appropriate form for a spatially filtered particle distribution function, which is dependent on an appropriately defined turbulent relaxation time. This concept is equivalent to Prandtl's mixing-length hypothesis, which suggests that the mean-free path of a fictive particle is affected by the local strain intensity.^{29,30} For this reason, the turbulent relaxation time τ_t is introduced into the effective relaxation time τ_w in order to take into account the effects of the small-scale turbulent fluid motion.

The incorporation of a SGS model into the LBM framework involves the introduction of a filtered discrete particle distribution function \overline{f}_i , defined as

$$\overline{f}_i(\vec{x} + \vec{c}_i \delta t, t + \delta t) - \overline{f}_i(\vec{x}, t) = -\frac{1}{\tau_w} [\overline{f}_i(\vec{x}, t) - \overline{f}_i^{eq}(\vec{x}, t)], \quad (28)$$

where τ_w is the effective relaxation time. The latter quantity can be written as

$$\tau_w = \tau_0 + \tau_t. \quad (29)$$

The total viscosity is then given by

$$\nu_w = \nu_0 + \nu_t, \quad (30)$$

where ν_0 is the kinematic viscosity and ν_t is the turbulent viscosity. The kinematic viscosity is determined from

$$\nu_0 = \left(\tau_0 - \frac{1}{2} \right) c_s^2 \delta t \quad (31)$$

and the turbulent viscosity assumes the form

$$\nu_t = \tau_t c_s^2 \delta t, \quad (32)$$

where δt is the time step.

In the LBM, the turbulent viscosity ν_t is determined with reference to the Smagorinsky SGS model as

$$\nu_t = C^2 \Delta^2 |\bar{S}|. \quad (33)$$

The effective relaxation time τ_w is related to the total viscosity ν_w by the following relation:

$$\tau_w = \frac{1}{2} + \frac{\nu_w}{c_s^2 \delta t} = \frac{1}{2} + \frac{1}{c_s^2 \delta t} (\nu_0 + \nu_t) = \frac{1}{2} + \frac{1}{c_s^2 \delta t} (\nu_0 + C^2 \Delta^2 |\bar{S}|). \quad (34)$$

Substituting Equation (31) into Equation (34), the effective relaxation time τ_w becomes

$$\tau_w = \tau_0 + \frac{C^2 \Delta^2}{c_s^2 \delta t} |\bar{S}|. \quad (35)$$

To proceed further, the resolved strain-rate tensor $\bar{S}_{\alpha\beta}$ is recast in terms of the nonequilibrium stress tensor $\bar{Q}_{\alpha\beta}$ (of the KT LBM model) as

$$\bar{S}_{\alpha\beta} = \frac{1}{2\rho_0 c_s^2 \tau_w} \bar{Q}_{\alpha\beta}. \quad (36)$$

The nonequilibrium stress tensor can be estimated directly from the filtered discrete particle distribution function \bar{f}_i as

$$\bar{Q}_{\alpha\beta} = \sum_{i=0}^{Q-1} c_{i,\alpha} c_{i,\beta} (\bar{f}_i - \bar{f}_i^{eq}). \quad (37)$$

The magnitude of the nonequilibrium stress tensor $|\bar{Q}|$ (defined in terms of $\bar{Q}_{\alpha\beta}$ analogously to how the magnitude of the resolved strain-rate tensor $|\bar{S}|$ is defined in terms of $\bar{S}_{\alpha\beta}$) is related to $|\bar{S}|$ as

$$|\bar{S}| = \frac{|\bar{Q}|}{2\rho_0 c_s^2 \tau_w}. \quad (38)$$

Substituting Equation (38) into Equation (35) results in a quadratic equation for the determination of τ_w given by

$$\tau_w^2 - \tau_0 \tau_w - \frac{C^2 \Delta^2}{2\rho_0 c_s^4 \delta t} |\bar{Q}| = 0. \quad (39)$$

Solving this equation for τ_w yields the following explicit expression for the effective relaxation time:

$$\tau_w = \frac{1}{2} \left(\sqrt{\tau_0^2 + \frac{2C^2 \Delta^2}{\rho_0 c_s^4 \delta t} |\bar{Q}|} - \tau_0 \right). \quad (40)$$

The effective relaxation time τ_w of equation (40) is used to define the BGK collision term in the LBE for the filtered discrete particle distribution function (cf. Equation (28)).

5 | FLOW PREDICTIONS

The LBM for compressible flow is validated using two test cases: isothermal and nonisothermal compressible-free jet flow using two LBM models in conjunction with LES. The two LBM model are (1) incorporation of a higher order expansion of

FIGURE 3 Schematic of the round jet nozzle and coordinate reference system [Colour figure can be viewed at wileyonlinelibrary.com]

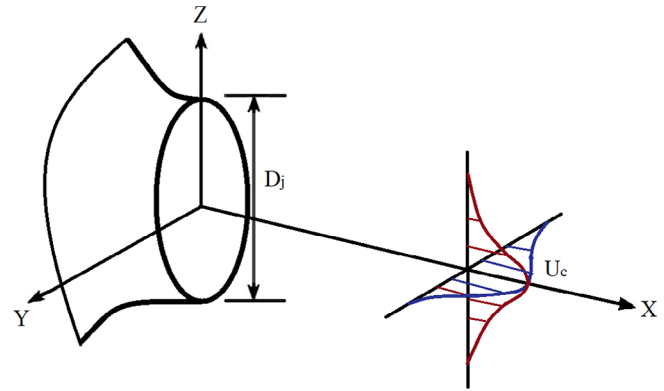


TABLE 1 Free circular jet characteristics and summary of spatial-temporal discretization

Test case characteristics	
Jet diameter	$D_j = 0.0508 \text{ m}$
Jet nozzle exit velocity	$U_j = 130, 170, 205 \text{ m s}^{-1}$
Kinematic viscosity	$\nu = 1.516 \times 10^{-5} \text{ m}^2 \text{ s}^{-1}$
Reynolds number	$Re \equiv (U_j D_j) / \nu = 4.35 \times 10^5, 5.7 \times 10^5$
Mach number	$Ma \equiv U_j / c = 0.4, 0.5, 0.6$
Physical dimensions (m)	LBM dimensions
$\Delta x = 0.0020833, \Delta y = 0.00127, \Delta z = 0.00127$	$\Delta x_{\text{lbm}} = \Delta y_{\text{lbm}} = \Delta z_{\text{lbm}} = \Delta t_{\text{lbm}} = 1$
$CFL = u \Delta t / \Delta x = 1 / (\sqrt{3} \cdot Ma) = 0.23$	Time step $\Delta t = CFL \cdot \Delta x / U_j = 0.5 \times 10^{-5} \text{ s}$
Total number of time steps	44,000

the equilibrium distribution function in the LBM and (2) use of the KT LBM. These two LBM models will be used for the simulation of an isothermal and a nonisothermal round jet flow at a Mach number of 0.5. The results of these simulations will be validated against some available experimental data reported by Bridges and Wernet³¹ and Laurendeau et al.³² and against some numerical data reported by Lew et al.¹⁵ for isothermal and nonisothermal jets. The experimental and numerical data provide measurements of the axial mean velocity $U_c(x)$ and the streamwise turbulence intensity $u_{rms}(x)$ as a function of the normalized streamwise distance x/D_j along the jet axis (D_j is the jet nozzle diameter).

Figure 3 provides a schematic of the round (axisymmetric) jet nozzle with reference to the coordinate system used to describe the geometry. Here, U_c is the mean streamwise velocity along the centerline of the jet ($y = z = 0$). The physical properties and flow characteristics for the subsonic jet flow simulations reported in this article are summarized in Table 1. Furthermore, Table 1 summarizes information on the discretization of the simulation domain and documents the details required to map the physical properties of the system to the nondimensional lattice units in which either the LBM–LES or KT–LBM–LES simulations were conducted. The domain size used for the simulations is $30D_j \times 13D_j \times 13D_j$ and each voxel grid cell in the uniform grid had physical dimensions of Δx , Δy , and Δz (see Table 1) in the x -, y -, and z -directions, respectively. The spatial domain of the LBM–LES simulations were conducted on a regular lattice (either D3Q19 for the LBM–LES simulations or D3Q15 for the KT–LBM–LES simulations) so that the curved boundaries of the round jet nozzle are not aligned with the lattice nodes. As a consequence, a staircase approximation was used for the representation of the curved surface of the round jet nozzle. Non-reflecting-type boundary conditions were imposed at the inlet, lateral, and outflow boundaries.³³

5.1 | Simulations using a higher order equilibrium distribution function (LBM–LES)

5.1.1 | Isothermal compressible-free jet flow

Figure 4 exhibits our LBM–LES predictions for the development of the mean normalized streamwise velocity $U_c(x)/U_j$ of an isothermal round jet at Mach number $Ma = 0.5$ as a function of the normalized downstream distance x/D_j along the

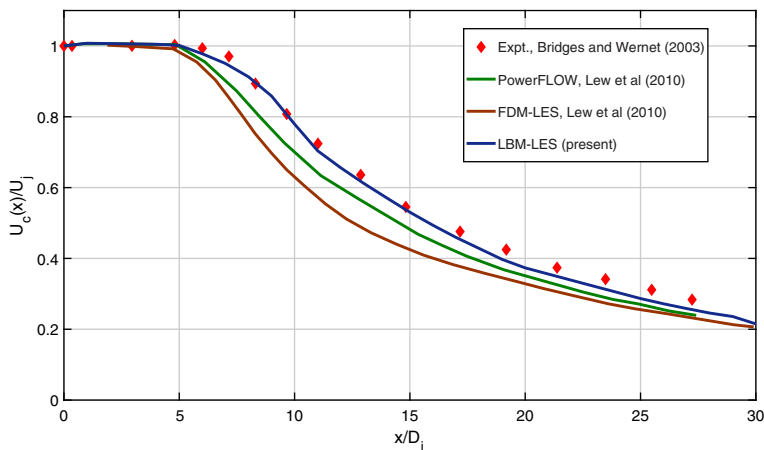


FIGURE 4 Development of the mean streamwise velocity along the centerline of an isothermal round jet for a Mach number $Ma = 0.5$ [Colour figure can be viewed at wileyonlinelibrary.com]

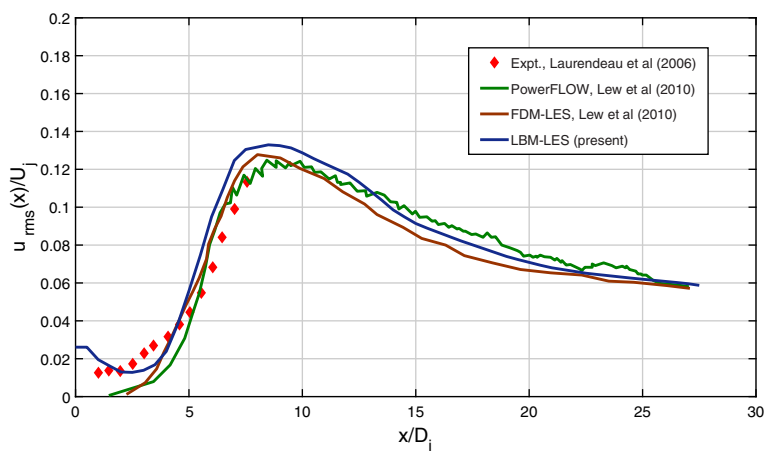


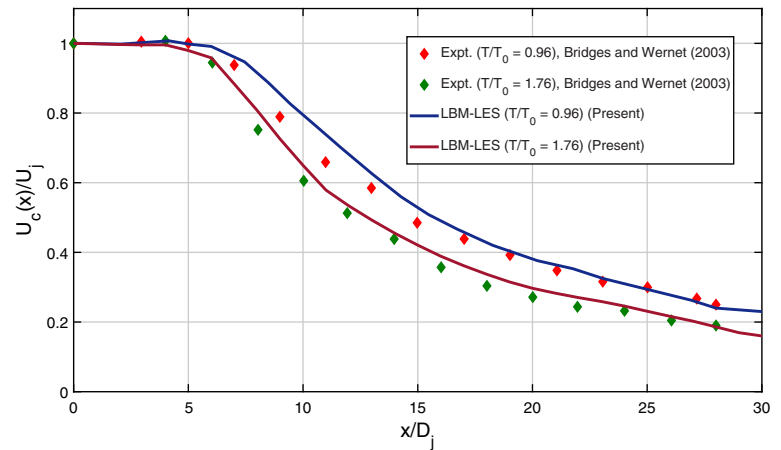
FIGURE 5 Development of the streamwise turbulence intensity along the centerline of an isothermal round jet for a Mach number $Ma = 0.5$ [Colour figure can be viewed at wileyonlinelibrary.com]

centerline of the jet, where U_j is the exit velocity at the jet nozzle and D_j is the jet diameter. These results are compared with some numerical simulations conducted by Lew et al.¹⁵ using a large-eddy simulation based on a finite difference discretization (FDM-LES) and an LBM simulation using the commercial code PowerFLOW developed by Exa Corporation (now Dassault Systemes). In addition, these numerical results are also compared with some experimental data obtained by Bridges and Wernet.³¹

Interestingly, our current LBM-LES predictions using the higher order equilibrium distribution function are in better conformance with the experimental data than the numerical results reported by Lew et al.¹⁵ More specifically, our current predictions agree very well with the experimental measurements provided by Bridges and Wernet,³¹ whereas the numerical simulations conducted by Lew et al.¹⁵ generally underpredict the experimental data, with the underprediction of the FDM-LES results being much more severe than that provided by the LBM simulation conducted using PowerFLOW. For downstream fetches $x/D_j > 5$, the mean streamwise velocity along the jet centerline decays roughly as x^{-1} and this rate of decay is correctly predicted using our LBM-LES model. Finally, for $x/D_j < 5$, the mean streamwise velocity $U_c(x)$ at the centerline is equal to the jet nozzle exit velocity U_j and this feature of the mean flow is captured well by all the predicted results (e.g., LBM-LES, FDM-LES, and PowerFLOW). In this regime of streamwise development, the fluid issuing from the jet nozzle (viz., vorticity generated inside of the nozzle and then swept downstream) remains relatively intact in the sense that the convoluted outer edge of the jet core has not had time to entrain (engulf) the external irrotational fluid (resulting in the growth of the jet diameter).

Figure 5 displays our LBM-LES predictions of the downstream development of the normalized streamwise turbulence intensity (normalized by the nozzle jet velocity U_j) along the centerline of the jet at a Mach number of $Ma = 0.5$. These predictions have been compared with similar numerical results obtained by Lew et al.¹⁵ using a finite difference LES code (FDM-LES) and the commercial LBM code PowerFLOW. These numerical results are also compared with some experimental data for the streamwise turbulence intensity for an isothermal round jet obtained at a Mach number $Ma = 0.3$ by Laurendeau et al.³²

FIGURE 6 The effects of temperature on the downstream development of the normalized mean streamwise velocity along the centerline of a heated round jet for a Mach number $Ma = 0.5$ [Colour figure can be viewed at wileyonlinelibrary.com]



For $x/D_j > 5$, the predictions of the streamwise turbulence intensity provided by LBM-LES, FDM-LES, and PowerFLOW are generally in good agreement with the experimental measurements, albeit the simulations are seen to slightly overestimate the streamwise turbulence intensity over this range of downstream fetches. For downstream fetches in the range $x/D_j < 5$, the LBM-LES predictions of $u_{rms}(x)$ are in better conformance with the experimental data than the predictions provided by FDM-LES and PowerFLOW. All three numerical models predict that the normalized streamwise turbulence intensity attains a peak value at a normalized downstream distance x/D_j of about 8 and decreases with increasing downstream fetch thereafter. Furthermore, all three numerical simulations predict a similar rate of decrease of the streamwise turbulence intensity with increasing downstream fetch for $x/D_j > 8$. Finally, over the range of downstream fetches x/D_j between about 5 and 8, the streamwise turbulence intensity is seen to increase with increasing downstream distance. In this regime of development, the entrainment of the ambient fluid into the jet (viz., the external irrotational fluid is engulfed into the core of the jet through its increasingly convoluted outer edge) results in the increase of the local intensity of the turbulent fluctuations in the jet.

5.1.2 | Nonisothermal compressible-free jet flow

The LBM-LES model that uses a higher order expansion of the equilibrium distribution is applied to the simulation of a nonisothermal and compressible-free jet flow. This objective here is to assess whether it is possible to apply this model to predict the effect of temperature on the downstream development of the mean streamwise velocity and the streamwise turbulence intensity along the centerline of the round jet. For this application involving a nonisothermal jet, all the terms in the sixth-order expansion of the equilibrium distribution function given in Equation (9) that depends on the temperature T need to be retained. To this purpose, the full-equilibrium distribution function of Equation (9) was incorporated into the LBM-LES model and used to provide simulations of the jet flow for two temperatures; namely, $T/T_0 = 0.96$ and $T/T_0 = 1.76$, where T_0 is a reference temperature (note that T in Equation (9) is nondimensional and is identified with T/T_0 here).

Figure 6 shows our LBM-LES predictions for the downstream development of the normalized mean streamwise velocity $U_c(x)/U_j$ as a function of the normalized downstream distance x/D_j along the jet centerline of a heated round jet at Mach number $Ma = 0.5$ for two normalized temperatures $T/T_0 = 0.96$ and 1.76 . These predictions are compared against some experimental data obtained by Bridges and Wernet.³¹ In general, it is seen that the LBM-LES predictions for the mean streamwise velocity is in very good agreement with the experimental measurements, especially at the higher temperature of $T/T_0 = 1.76$. At the lower temperature of $T/T_0 = 0.96$, it is seen that the LBM-LES predictions slightly overestimate the mean streamwise velocity for downstream fetches $10 < x/D_j < 15$. It is noted that the rate of decay of the mean streamwise velocity along the jet centerline is larger for the heated jet at $T/T_0 = 1.76$ in comparison with that at $T/T_0 = 0.96$. This physical effect is correctly predicted by the LBM-LES model. At the higher temperature, the density of jet fluid is reduced relative to the density of the ambient fluid resulting in an increased entrainment of the ambient irrotational fluid into the jet through the convoluted outer jet boundary resulting in a larger spreading rate leading to an increased jet width and a concomitant reduction in the mean streamwise velocity (in comparison with the heated jet at the lower temperature).

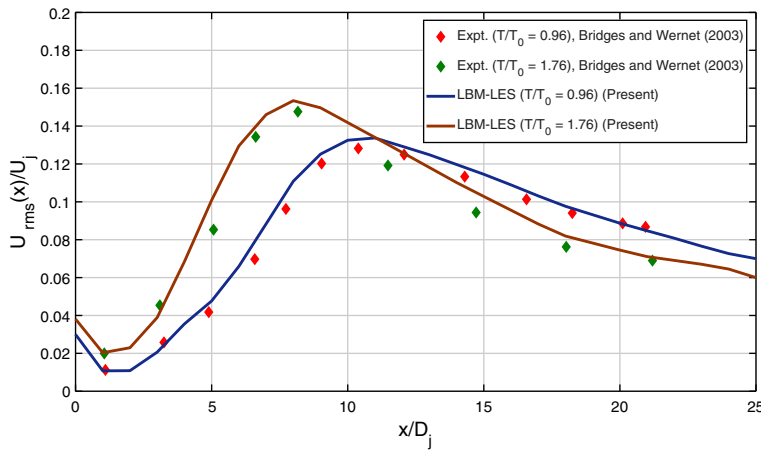


FIGURE 7 The effects of temperature on the downstream development of the normalized streamwise turbulence intensity along the centerline of a heated round jet for a Mach number $Ma = 0.5$ [Colour figure can be viewed at wileyonlinelibrary.com]

In a similar manner, Figure 7 exhibits our LBM-LES predictions of the downstream evolution of the normalized streamwise turbulence intensity $u_{rms}(x)/U_j$ as a function of the normalized downstream distance x/D_j for a heated round jet at Mach number $Ma = 0.5$ for two normalized temperatures $T/T_0 = 0.96$ and 1.76 . It is noted that our LBM-LES predictions for the streamwise turbulence intensity are in excellent conformance with some experimental measurements obtained by Bridges and Wernet.³¹ The temperature of the heated jet has a significant effect on the streamwise turbulence intensity and this physical effect is captured correctly by our LBM-LES simulations. In particular, note that over the range of downstream fetches from about $x/D_j = 3$ to 10 , the streamwise turbulence intensity is larger for the heated jet at the higher temperature. Here, the reduced jet density at the higher temperature results in a larger local shear at the outer boundary of the jet resulting in an increased turbulence (kinetic energy) production. The radial flux of this increased turbulence kinetic energy from the outer boundary of the jet (region of most intense turbulence) to that at the jet core (region of weaker turbulence) results in an increased level of streamwise turbulence intensity at the jet centerline for the heated jet at the higher temperature ($T/T_0 = 1.76$) relative to that at the lower temperature ($T/T_0 = 0.96$). These physical effects are well predicted by the LBM-LES model. Finally, the downstream location in the peak of the streamwise turbulence intensity is closer to the jet nozzle and attains a larger value for the jet at the higher temperature relative to that at the lower temperature. This observed variation in $u_{rms}(x)/U_j$ is well reproduced by the LBM-LES predictions.

5.2 | Simulations using the KT-LBM-LES model

In this subsection, the potential for large-eddy simulation of turbulent flow with the KT-LBM²¹ used in conjunction with the D3Q15 lattice model will be investigated in detail. To this purpose, the KT-LBM-LES will be used to provide detailed predictions for the subsonic flow dynamics associated with the compressible unheated and heated round jet flows. These predictions will be compared with some available experimental and numerical data.

5.2.1 | Isothermal compressible-free jet flow

Figure 8 exhibits the KT-LBM-LES predictions of the downstream evolution of the normalized mean streamwise velocity $U_c(x)/U_j$ as a function of the normalized downstream distance x/D_j along the centerline of an isothermal round jet at a Mach number of 0.5 . These predictions are compared with some experimental data obtained by Bridges and Wernet³¹ and some numerical simulations conducted by Lew et al.¹⁵ The latter simulations include a finite difference LES (FDM-LES) prediction as well as an LBM prediction obtained using the commercial code PowerFLOW. It is noted that all the numerical predictions (viz., KT-LBM-LES, FDM-LES, and PowerFLOW) underpredict the experimental measurements for the mean streamwise velocity for downstream fetches x/D_j greater than about 5 . The KT-LBM-LES predictions are comparable with the LBM predictions provided by PowerFLOW. The underprediction of $U_c(x)$ is most severe for FDM-LES. In spite of this, the predictions for the rate of decay of the mean streamwise velocity is in good agreement with the

FIGURE 8 Development of the mean streamwise velocity along the centerline of an isothermal round jet for a Mach number $Ma = 0.5$ [Colour figure can be viewed at wileyonlinelibrary.com]

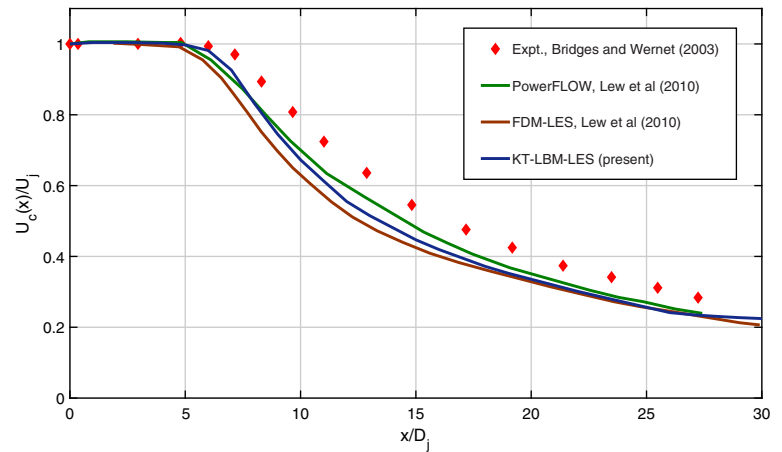
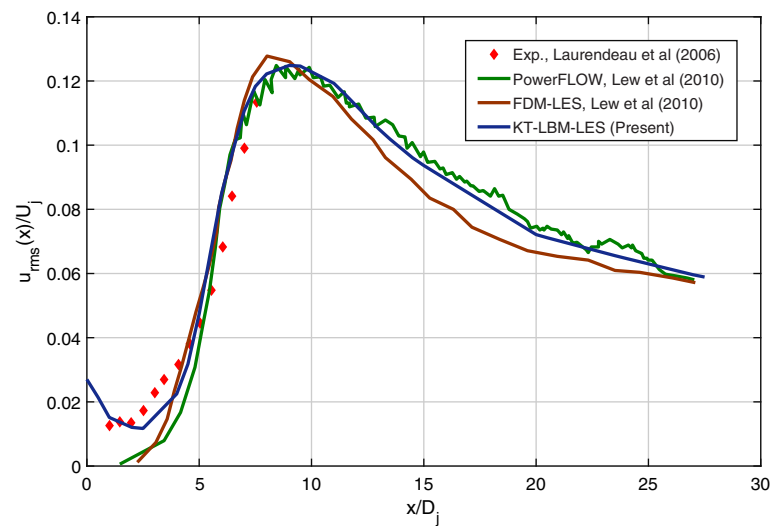


FIGURE 9 Development of the streamwise turbulence intensity along the centerline of an isothermal round jet for a Mach number $Ma = 0.5$ [Colour figure can be viewed at wileyonlinelibrary.com]



experimental observations. Finally, a comparison of Figure 8 with Figure 4 shows that the LBM-LES predictions for the mean streamwise velocity are in better agreement with the experimental measurements than those provided by the KT-LBM-LES.

Figure 9 shows the KT-LBM-LES predictions for the downstream development of the streamwise turbulence intensity along the centerline of the isothermal round jet. These predictions are compared with some experimental data reported by Laurendeau et al.³² as well as some numerical predictions obtained by Lew et al.¹⁵ Generally, the KT-LBM-LES predictions are in very good agreement with the experimental measurements over the range of downstream fetches for which data are available. The KT-LBM-LES predictions for the streamwise turbulence intensity are comparable with the LBM predictions provided by PowerFLOW, except for downstream fetches near the jet entrance region ($x/D_j < 5$) where it is seen that the KT-LBM-LES predictions are in better conformance with the experimental data than those provided by PowerFLOW. For $x/D_j > 15$, the FDM-LES predictions for the streamwise turbulence intensity are systematically smaller than the KT-LBM-LES and PowerFLOW predictions. As a further note, a perusal of Figures 5 and 9 suggests that the KT-LBM-LES predictions for the downstream evolution of the streamwise velocity are slightly better than those provided by the LBM-LES.

5.2.2 | Nonisothermal compressible-free jet flow

Figure 10 displays the KT-LBM-LES predictions for the downstream evolution of the normalized mean streamwise velocity along the jet centerline for a heated round jet at two temperatures; namely, $T/T_0 = 0.96$ and 1.76 . An examination of Figure 10 shows that the KT-LBM-LES predictions for $U_c(x)$ are generally in excellent conformance with the experimental

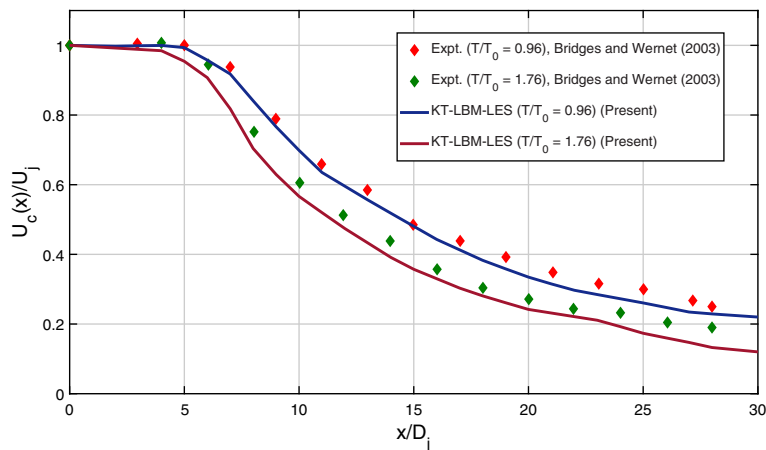


FIGURE 10 The effects of temperature on the downstream development of the normalized mean streamwise velocity along the centerline of a heated round jet for a Mach number of $Ma = 0.5$ [Colour figure can be viewed at wileyonlinelibrary.com]

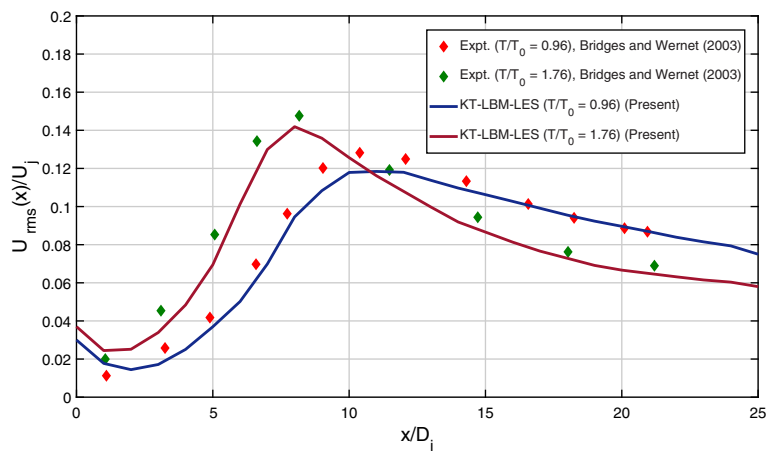


FIGURE 11 The effects of temperature on the downstream development of the normalized streamwise turbulence intensity along the centerline of a heated round jet for a Mach number $Ma = 0.5$ [Colour figure can be viewed at wileyonlinelibrary.com]

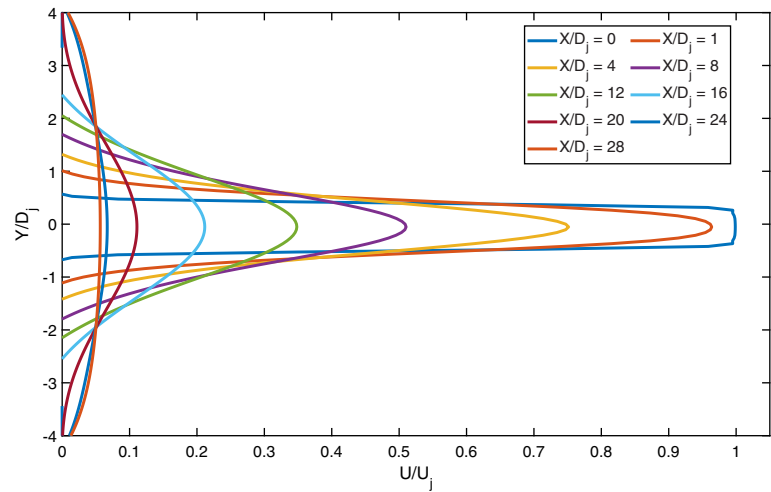
measurements obtained by Bridges and Wernet.³¹ A careful perusal of Figures 6 and 10 shows that the KT-LBM-LES and LBM-LES predictions for the mean streamwise velocity are comparable in quality. It is seen that the KT-LBM-LES slightly underpredicts $U_c(x)$ at the two temperatures, whereas the LBM-LES slightly overpredicts $U_c(x)$ at the two temperatures with the overpredictions being most severe in the downstream range x/D_j between about 6 and 12 for the lower temperature $T/T_0 = 0.96$. The differences in the predictions here probably stem from the different models used for the equilibrium distribution in LBM-LES (higher order expansion of the Maxwell-Boltzmann distribution) and KT-LBM-LES (circular distribution). The implication here (not surprisingly) is that the type of equilibrium distribution function used in the LBM plays a key role in the predictive performance of the model.

Figure 11 exhibits the KT-LBM-LES predictions for the downstream development of the normalized streamwise turbulence intensity along the centerline of a heated round jet at two different temperatures ($T/T_0 = 0.96$ and 1.76). These predictions are generally in good agreement with the experimental data obtained by Bridges and Wernet.³¹ Note that the KT-LBM-LES results underpredict the experimental measurements over a wide range of downstream fetches with the underprediction being most severe at the downstream location corresponding to the maximum of the streamwise turbulence intensity. By contrast, from Figure 7 it is seen that the comparable LBM-LES predictions for the streamwise turbulence intensity slightly overpredict the corresponding experimental measurements. As in the case of the mean streamwise velocity, it is apparent that these differences in the predictive performance of the KT-LBM-LES and LBM-LES results can be probably attributed to the different formulations for the equilibrium distribution functions used in these two models.

6 | NEAR-FIELD NOISE PREDICTIONS

Experimental measurements and numerical simulations have provided a deeper understanding of the physical characteristics of jet noise in both the near-field and far-field regimes. On the macroscopic scale, the lattice Boltzmann

FIGURE 12 Cross-stream profiles of the normalized mean streamwise velocity U/U_j at various downstream locations x/D_j along the centerline of an isothermal round jet at a Mach number $Ma = 0.5$ [Colour figure can be viewed at wileyonlinelibrary.com]



equations are equivalent to the continuity equation and the compressible Navier–Stokes equation and, as a consequence, the LBM/LES methodology provides a physically based methodology for the prediction of sound propagation in viscous turbulent fluids and, in particular, for the prediction of the acoustics associated with a subsonic turbulent jet flow in both the near-field and far-field regimes.

To this purpose, the pressure field provided by the LBM simulation is particularly relevant (cf. Equation (16)). More specifically, the maximum achievable Strouhal number for this type of simulation can be expressed as $St_{\max} = f_{\max} D_j / U_j = 2$, where the maximum frequency is determined as $f_{\max} = c_{\infty} / \lambda = 4000$ Hz. Here, c_{∞} is the speed of sound (which should not be confused with the “speed of sound” lattice constant c_s) and λ is the wavelength. This section will present results of the near-field noise characteristics associated with the jet flow simulated in the previous section (e.g., velocity and pressure fields, sound pressure level).

Figure 12 presents the cross-stream profiles of the normalized mean streamwise velocity at various downstream locations for the isothermal round jet at a Mach number $Ma = 0.5$. As can be seen, the uniform mean streamwise velocity near the exit of the nozzle evolves with increasing downstream fetch x/D_j as the shape of the velocity profiles transitions from the sharper square pulse shape near the nozzle to a more diffuse Gaussian shape further from the nozzle exit (as the jet evolves into the self-similar regime of development).

This development is consistent with the entrainment of the ambient irrotational fluid into the jet core through the convoluted outer edge of the jet, leading to the flow toward the jet that feeds its increasing girth (local jet width). This can be seen more clearly in Figure 13 which shows the isocontours for the instantaneous streamwise velocity (normalized by the velocity at the jet nozzle) in a horizontal (x - y) plane through the jet at a fixed time. Here, it is evident that the outer edge of the jet is convoluted and corresponds to the interface between two regions of the fluid representing a sudden transition from the turbulent vorticity field in the jet core to the external (ambient) irrotational fluid. In particular, the free shear layer between the high-vorticity flow in the jet core and the ambient fluid creates the convoluted outer edge of the jet, particularly for downstream fetches x/D_j greater than about 10 as illustrated in Figure 13.

Figure 14 displays the isocontours of the local Mach number $M_j = U/c_l$ in a horizontal cross-section through the isothermal round jet (where U is the time-averaged (mean) velocity and $c_l = \left(\gamma \frac{P}{\rho}\right)^{1/2}$ is the local speed of sound in the fluid and γ is the ratio of specific heats of the fluid). The local Mach number decreases with increasing x/D_j . At a fixed downstream fetch, the local Mach number decreases toward the outer boundary of the jet. In this region, an elliptic zone is created in the free shear layer corresponding to the continual engulfment (entrainment) of external irrotational fluid into the jet. This dragging of ambient fluid into the jet in this zone increases its mass flux and is responsible for most of the sound generation in the jet.

Figure 15 displays the isocontours for the dynamic pressure (sound) P (normalized by the pressure P_j at the jet nozzle) in a horizontal (x - y) cross-section through the isothermal round jet (at a Mach number of $Ma = 0.5$). As expected, the isopleths of the effective sound pressure P/P_j are similar to those for the velocity because the pressure is related to the velocity and density. The dynamic pressure relative to the pressure at the jet exit increases near the jet exit because that is the location where the mean velocity increases. Beyond the potential jet core, the pressure begins to decay gradually downstream as the velocity decays with increasing x/D_j .

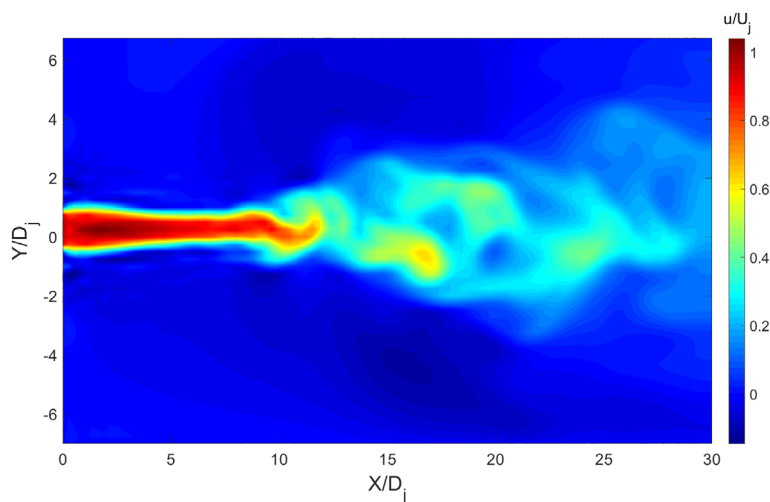


FIGURE 13 Isocontours of the instantaneous streamwise velocity for an isothermal round jet at a Mach $Ma = 0.5$ obtained in a horizontal plane through the jet flow at a fixed instant in time [Colour figure can be viewed at wileyonlinelibrary.com]

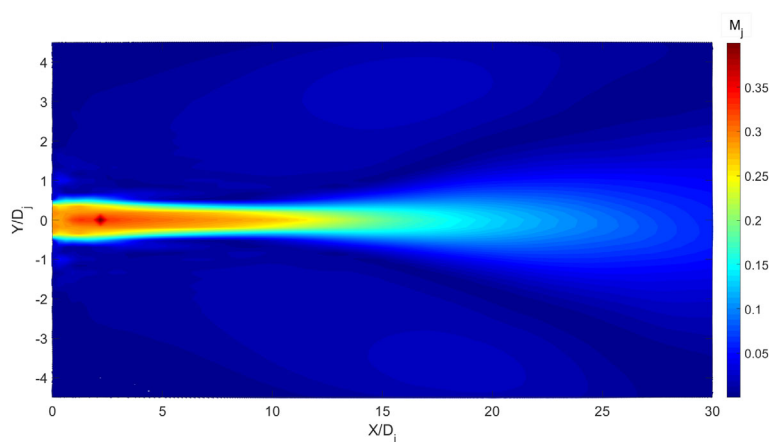


FIGURE 14 Isocontours of the local Mach number M_j in a horizontal (x - y) cross-section through the isothermal round jet at a Mach number $Ma = 0.5$ [Colour figure can be viewed at wileyonlinelibrary.com]

The dynamic pressure isocontours in Figure 15 shows that the pressure exhibits a sharp drop near the outer (free) shear layer region of the jet, where the entrainment of the ambient fluid occurs (involving the engulfment of the irrotational fluid through the convoluted outer edge of the jet). Outside this free shear layer zone, the radial (y) pressure gradient is much smaller than that inside the zone. Indeed, a low dynamic pressure zone appears outside the potential jet which is related to the low flow velocity outside the shear layer.³⁴ Furthermore, the axial (x) pressure gradient in the shear layer is larger, and this leads to the generation of sound in this layer. It is worth noting that the noise caused by the pressure gradient near the jet exit can be characterized as originating from a monopole sound source.

Figure 16 displays isocontours of the sound pressure level $SPL \equiv 20 \log_{10} \left(\frac{p}{p_{ref}} \right)$ in a horizontal (x - y) cross-section through the isothermal round jet. Here, the reference pressure is chosen to be $p_{ref} = 20 \times 10^{-5}$ Pa and corresponds to the absolute threshold of hearing (minimum sound level that can just be heard by an average human). The sound pressure level decays gradually in the downstream direction and remains at a high level inside the jet shear layer cone. Outside the core region, the jet flow zone associated with the dark yellow contours in Figure 16 corresponds to a zone of intermediate sound pressure levels. Between these two zones, the downstream propagation of high-frequency sound waves in the developing zone generates a thin layer of very low sound pressure level outside the shear layer, known as the “cone of silence.”³⁵

Figure 17 exhibits the downstream development of the sound pressure level SPL (up to a downstream fetch of $x/D_j = 30$) at three different cross-stream (radial) positions in the isothermal round jet, namely at $y/D_j = 0, 0.5$ and 1.0 . Along the centerline of the jet (at $y/D_j = 0$), the predicted sound pressure level obtained in our LBM-LES simulations is seen to decrease linearly (approximately or better) with increasing downstream fetch. This predicted behavior of the SPL is in good conformance with some experimental results obtained by Mancinelli et al.³⁶ for a subsonic

FIGURE 15 Isocontours of the normalized sound pressure P/P_j in a horizontal (x - y) cross-section through an isothermal round jet at a Mach number $Ma = 0.5$ [Colour figure can be viewed at wileyonlinelibrary.com]

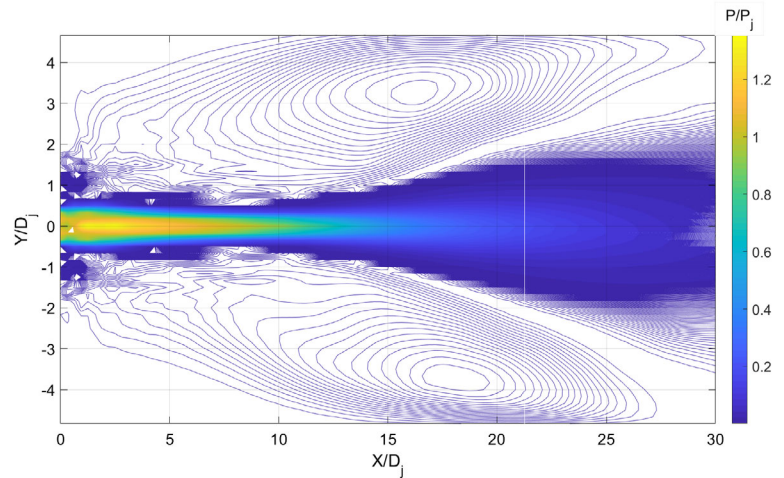
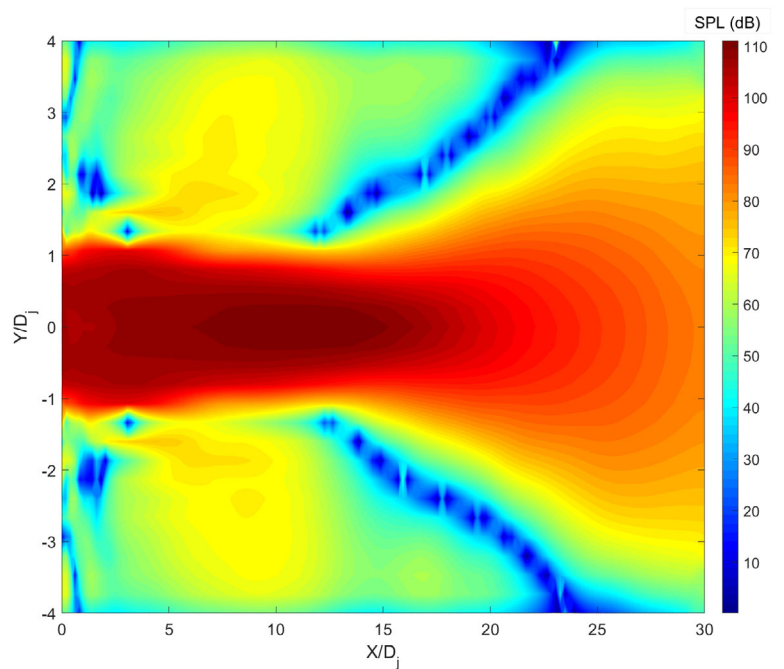


FIGURE 16 Isocontours of the sound pressure level SPL (dB) in a horizontal (x - y) cross-section through an isothermal round jet at a Mach number $Ma = 0.5$ [Colour figure can be viewed at wileyonlinelibrary.com]



jet flow at a Mach number of 0.6. The downstream variation of the SPL for locations off the centerline of the jet is much more complex. For example, at the radial location $y/D_j = 1.0$, the SPL increases from the jet nozzle at $x/D_j = 0$ to a local maximum at $x/D_j \approx 5.0$ and then decreases rapidly from this point until it attains a local (absolute) minimum at a downstream fetch of $x/D_j \approx 14.0$ corresponding to the region associated with the “cone of silence.” Beyond the “cone of silence,” the SPL begins to increase again to reach an SPL of about 70 dB at the downstream location $x/D_j = 30$.

7 | FAR-FIELD NOISE PREDICTIONS

Most flow noise problems require a hybrid solution involving two steps: first, the governing equations for the flow in the near-field must be solved numerically, and second, a wave equation must be used to predict the far-field noise using the near-field flow properties as sources. The numerical solution of these types of problems is computationally expensive and requires high-performance computing.³⁷ The Kirchhoff–Helmholtz integral methodology, which is widely used for the solution of acoustics problems, allows the sound pressure in the surrounding region to be determined from knowledge of the sound pressure and velocity on a control surface. This methodology was developed as a means to investigate light

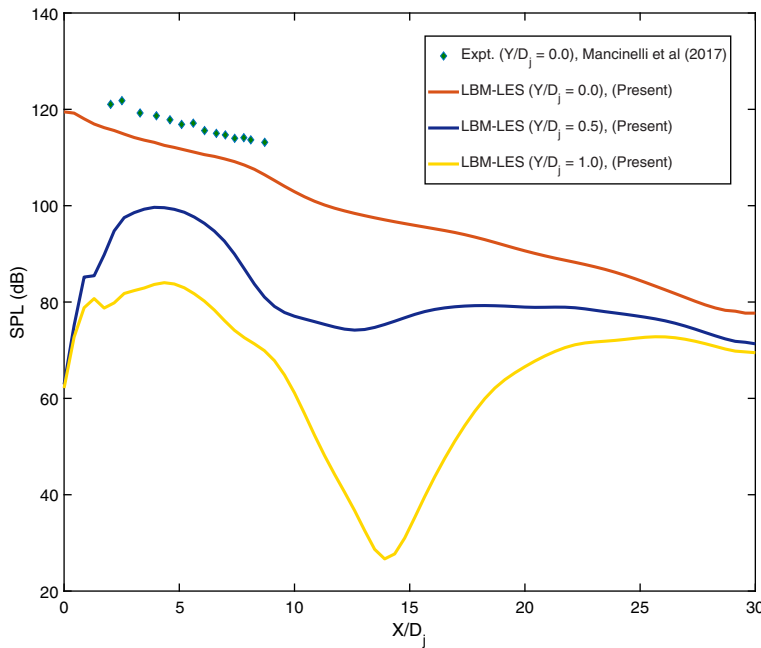


FIGURE 17 Downstream development of the sound pressure level (SPL) in dB at three different cross-stream (radial) locations in an isothermal round jet at a Mach number $Ma = 0.5$ [Colour figure can be viewed at wileyonlinelibrary.com]

diffraction and electromagnetic waves, but was later modified for aeroacoustics applications such as fan noise, wind turbines, and jet noise.

In this article, we apply the Kirchhoff–Helmholtz integral methodology to predict the noise in the far field of a subsonic jet. To this purpose, Figure 18 shows a Kirchhoff control surface around the jet. For a free jet flow, the pressure field around the jet can be expressed in terms of the following surface integral:³⁸

$$p(x, y, z, t) = -\frac{1}{4\pi} \int \left[\frac{p}{r_0^2} \frac{\partial r_0}{\partial n_0} + \frac{1}{r_0} \frac{\partial p}{\partial n_0} + \frac{1}{c_\infty r_0 \beta^2} \frac{\partial p}{\partial t} \left(\frac{\partial r_0}{\partial n_0} - M_\infty \frac{\partial \hat{x}_0}{\partial n_0} \right) \right] dS_0, \quad (41)$$

where

$$x_0 = x, \quad y_0 = y\beta, \quad z_0 = z\beta, \quad (42)$$

$$r_0 = ((x - \hat{x})^2 + \beta^2[(y - \hat{y})^2 + (z - \hat{z})^2])^{1/2}, \quad (43)$$

$$\beta = (1 - M_\infty^2)^{1/2}, \quad (44)$$

and

$$\tau = \frac{[r_0 - M_\infty(x - \hat{x})]}{c_\infty \beta^2}. \quad (45)$$

Here, r_0 is the distance between the noise source and the field point, M_∞ is the free-stream Mach number, c_∞ is the speed of sound in the free-stream, $\tau \equiv t - \hat{\tau}$ is the retarded time, n_0 is the outward normal to the Kirchhoff control surface, and S_0 is the Kirchhoff control surface.

Using the pressure and velocity of the flow on the Kirchhoff control surface obtained from the compressible LBM–LES jet simulation enables the noise to be obtained at any field point located in the region outside the Kirchhoff control surface (and, more particularly, in the far field of the jet). Pan et al.³⁹ proved that the control surface (see Figure 18) must surround the entire source region of the jet in order for the Kirchhoff–Helmholtz integral methodology to provide efficient and accurate predictions of the noise generated from the turbulent flow.

Figure 19 shows the spectra of the fluctuating streamwise velocity at a downstream distance of $x = 10D_j$ at the center-line of an isothermal round jet. The streamwise velocity spectrum obtained from our LBM–LES simulation is in very good agreement with that obtained using PowerFLOW¹⁵ (a pure LBM simulation). However, it is seen that these two spectra

FIGURE 18 Kirchhoff control surface used to predict the noise in the far field of a jet [Colour figure can be viewed at wileyonlinelibrary.com]

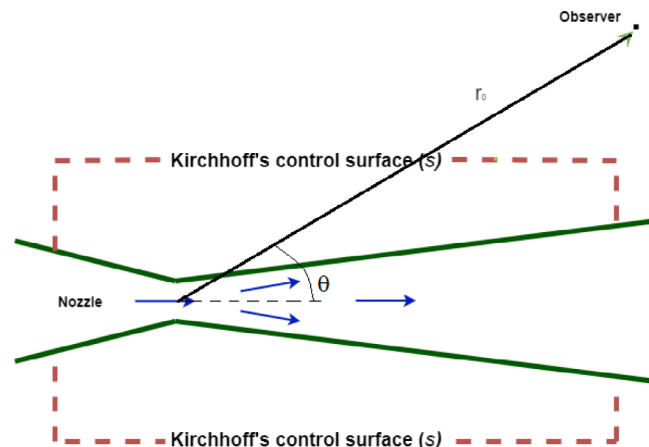
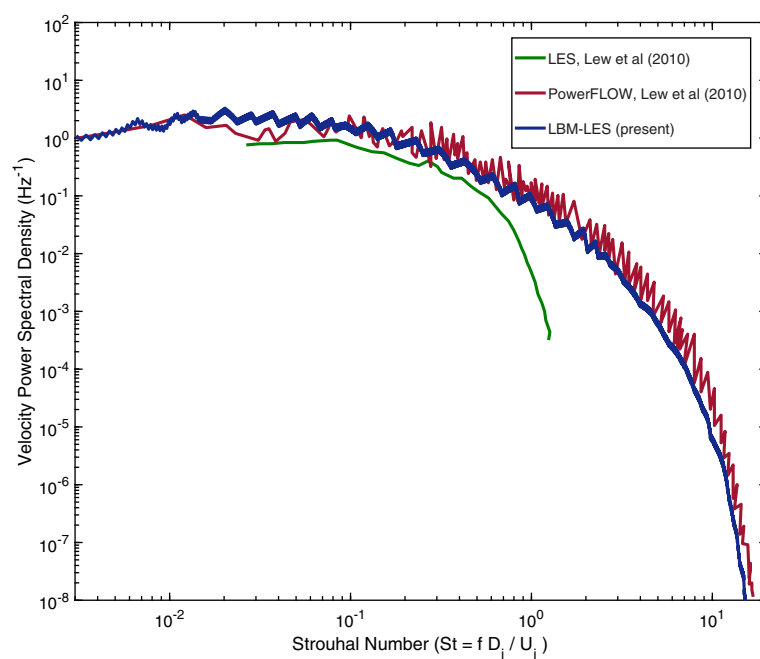


FIGURE 19 Power spectra of the streamwise velocity (normalized by the jet nozzle velocity U_j) at a downstream distance of $x = 10D_j$ along the centerline of an isothermal round jet at Mach number $Ma = 0.5$ [Colour figure can be viewed at wileyonlinelibrary.com]



obtained using LBM simulations deviate slightly from the power spectrum obtained by Lew et al.¹⁵ using LES, with the deviation being the most severe at the higher frequencies. In particular, the LBM simulations here were able to better resolve the smaller scales of the turbulent jet flow than the simulation obtained using the coarse-resolution LES.

LBM-LES can be used for the prediction of noise generated in turbulent flows in both the near and far field (the latter in conjunction with the Kirchhoff-Helmholtz integral methodology). As an example of the far-field prediction of the noise generated by a subsonic jet, Figure 20 shows the directivity pattern of the overall sound pressure level (OASPL) at a far-field point located at a distance of $r_0 = 72D_j$ from an isothermal round jet for an azimuthal angle ϕ of zero degrees (i.e., along the jet or x -axis) and for a range of elevation angles θ from 15° to 90° (positive when measured above the x - y plane—cf. Figure 18). The OASPL at these far-field locations were predicted using a hybrid LBM-LES-Kirchhoff methodology. The predictions show that the sound pressure levels increase with increasing elevation angle, reaching a peak value of about 85 dB for elevation angles θ between about 30° and 60° , where the jet flow exhibits a high-turbulence-intensity. Furthermore, these predictions can be compared with some experimental measurements obtained by Tanna.⁴⁰ The predicted OASPL deviates from the experimental measurements by less than about 2 dB for elevation angles in the range from $\theta = 15^\circ$ to 90° . Finally, Figure 20 also displays a numerical prediction for the OASPL obtained by Tanna⁴⁰ using the Lighthill analogy.⁴¹ These numerical predictions are in good conformance with those obtained from the LBM-LES-Kirchhoff methodology for elevation angles θ greater than about 50° , but significantly overestimate the OASPL at smaller elevation angles (viz., for θ less than about 40°).

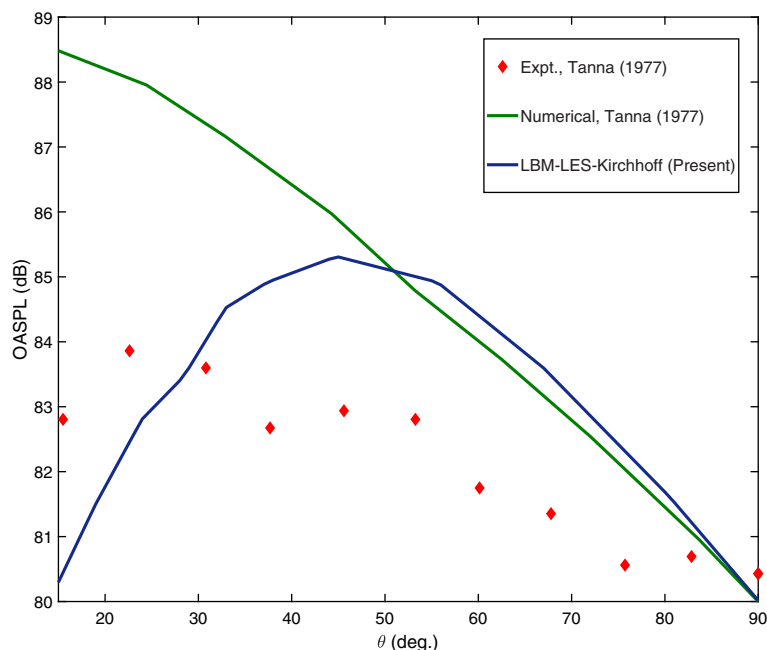


FIGURE 20 Directivity of the overall sound pressure level (OASPL) at a distance $r_0 = 72D_j$ from an isothermal round jet at Mach number $Ma = 0.5$. The predictions are along the jet (x) axis (azimuthal angle $\phi = 0$) for a range of elevation angles θ between 15° and 90° (where the elevation angle is measured relative to the horizontal x - y plane) [Colour figure can be viewed at wileyonlinelibrary.com]

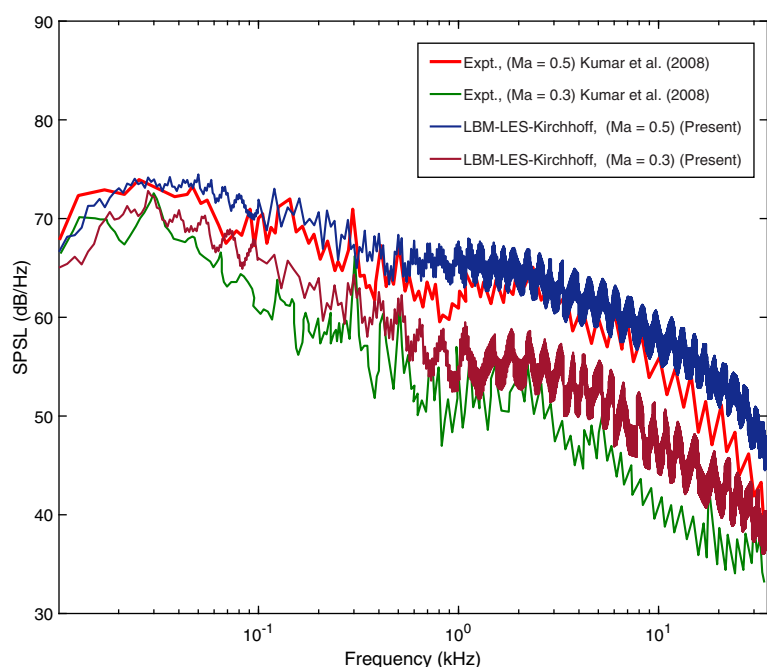
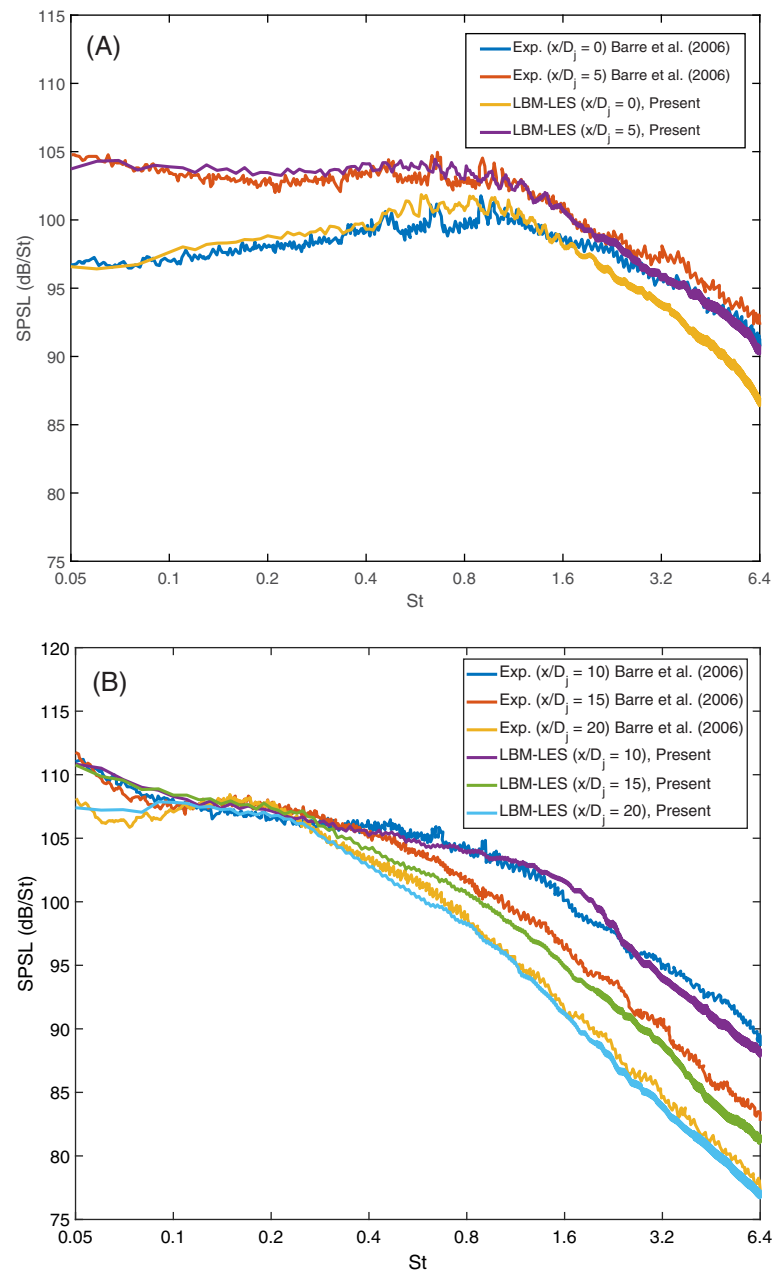


FIGURE 21 Predicted and experimental sound pressure spectrum level (SPSL) for an isothermal round jet at Mach numbers $Ma = 0.3$ and 0.5 obtained at $x = 0$ and $r \equiv Y = 10D_j$ [Colour figure can be viewed at wileyonlinelibrary.com]

Figure 21 displays the SPL power spectra (or, equivalently, the sound pressure spectrum level [SPSL]) for an isothermal round jet at Mach numbers $Ma = 0.3$ and 0.5 predicted using the LBM-LES-Kirchhoff methodology. The SPL power spectra were obtained at $x = 0$ for a fixed radial (cross-stream) location of $r \equiv Y = 10D_j$ corresponding to the near-field regime. The predicted sound pressure spectra exhibit distinct peaks. As the numerical results predict, the sound pressure spectra exhibit distinct peaks at the lower frequencies owing to the fact that the pressure fluctuations are steadier at smaller amplitudes. At the higher frequencies, however, the pressure fluctuations are characterized by larger amplitudes and, in consequence, generate larger sound pressure spectra variations as the frequency increases. The sound pressure spectra at the lower frequencies are associated with the strong tones of the jet flow field. Figure 21 also exhibits experimental measurements of the SPL power spectra for a round jet at Mach numbers of 0.3 and 0.5 obtained by Kumar et al.⁴² It is evident that the predicted SPL power spectra at $x = 0$ and $r \equiv Y = 10D_j$ are in very good conformance with the associated experimental measurements.

FIGURE 22 Predicted and experimental sound pressure level spectra for an isothermal round jet at a Mach number $Ma = 0.6$ obtained at a fixed radial (cross-stream) location $y/D_j = 7.5$ and at axial locations (a) $x/D_j = 0$ and 5 (near-field regime) and (b) $x/D_j = 10, 15, 20$ (far-field regime) [Colour figure can be viewed at [wileyonlinelibrary.com](https://onlinelibrary.wiley.com/doi/10.1002/fla.4914)]



As a further validation of our hybrid approach for computational aeroacoustics involving a subsonic turbulent jet flow, Figure 22 compares the sound pressure level power spectra (SPSL) with some experimental measurements obtained by Barre et al.⁴³ in both the near-field and far-field acoustic regimes of the jet. More specifically, the SPSL was predicted using our LBM/LES and Kirchhoff–Helmholtz integral methodology (for far-field noise prediction) for a subsonic round jet flow at a Mach number $Ma = 0.6$ at a fixed radial (cross-stream) distance from the jet centerline of $y/D_j = 7.5$ at jet axial locations of $x/D_j = 0, 5, 10, 15$, and 20 . The SPSL in Figure 22 are exhibited as a function of the normalized frequency $St \equiv fD_j/U_j$ (Strouhal number) at locations in both the near-field (cf. Figure 22(A)) and far-field (cf. Figure 22(B)) regimes. The predictions of the SPSL are in very good conformance with the experimental measurements and imply that the hybrid approach for computational aeroacoustics used herein is able to predict the streamwise development of the SPSL well.

For sound pressure spectrum levels in the near-field acoustic regime (cf. Figure 22(A)), the spectra exhibit a weak spectral peak at a Strouhal number St of about 0.6 . At greater downstream distances from the jet nozzle, the pressure spectra do not exhibit clear-cut spectral energy peak (cf. Figure 22(B)). Indeed, moving downstream from the jet nozzle in the range $10 \leq x/D_j \leq 20$, the pressure spectra evolves into a broadband energy spectrum where the energy decay is

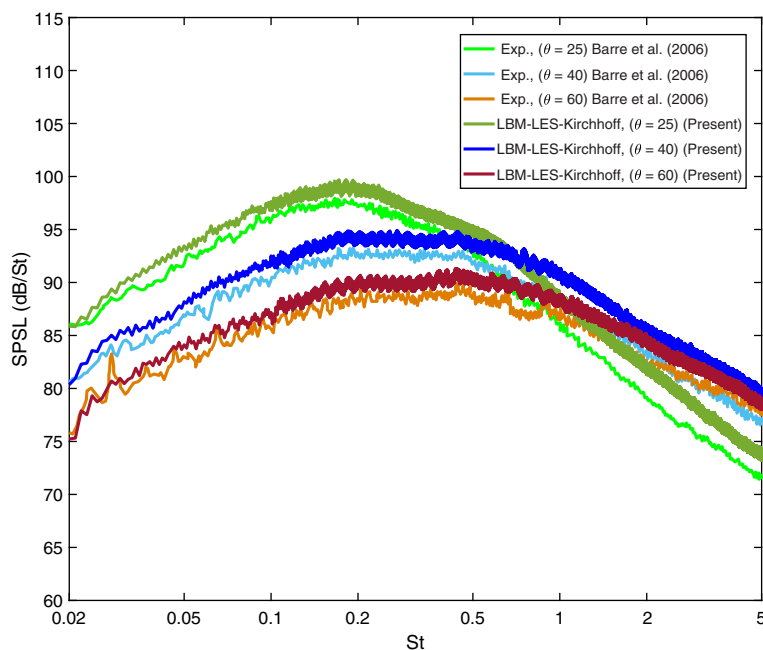


FIGURE 23 Predicted and experimental sound pressure level spectra for an isothermal round jet at a Mach number $Ma = 0.6$ obtained at a fixed radial distance $r_0/D_j = 52$ from the center of the jet nozzle for three different values of the azimuthal angle θ [Colour figure can be viewed at wileyonlinelibrary.com]

smaller at the lower frequencies than that at the higher frequencies. The characteristic frequency corresponding to the transition from the smaller to the larger energy decay rate in the pressure spectra moves toward lower frequencies with increasing downstream distance from the jet nozzle. Furthermore, in the range of frequencies associated with the higher energy decay, the spectral energy levels at any given value of the Strouhal number decrease monotonically with increasing axial distance.

As a final illustration of the validation of the proposed hybrid LBM/LES and Kirchhoff integral methodology for computational aeroacoustics, Figure 23 shows our model predictions of the SPL in the very far-field regime for a subsonic isothermal jet flow with a Mach number $Ma = 0.6$ at a fixed radial distance $r_0/D_j = 52$ (cf. Figure 18) from the center of the jet nozzle at three different azimuthal angles, namely, at $\theta = 25^\circ$, 40° , and 60° . The predicted pressure spectra are compared with some experimental data obtained by Barre et al.⁴³ It is noted that the predicted pressure spectra are in excellent agreement with the measured pressure spectra. More specifically, the predicted sound pressure spectrum levels slightly overestimate the measured spectrum levels, and this overestimation is no larger than 3 dB over the frequency range for which measurements are available. The broad energy hump in the pressure spectra moves from a lower to higher frequency range as the azimuthal angle θ from the jet axis increases. This evolution in the pressure spectral shape as a function of the azimuthal angle from the jet axis is predicted correctly by the model.

8 | CONCLUSIONS

We have investigated the applicability of a compressible LBM with a subgrid-scale turbulence model for the simulation of turbulent subsonic fluid flow. The essential concept underpinning the inclusion of a subgrid-scale turbulence model in a compressible LBM is based on the assumption that all of the physical effects that the unresolved motions have on the resolved fluid motion can be parameterized by a heuristic model that is based on variables that can be predicted.⁵

The numerical results obtained with the compressible LBM using either a higher order expansion for the equilibrium particle distribution or the KT model in conjunction with LES for subsonic isothermal and nonisothermal round jet flows (at various jet Mach numbers Ma) showed very good agreement with both previous numerical simulations and available experimental measurements. The predictions obtained with either the proposed LBM-LES or KT-LBM-LES methodologies for the mean velocity and turbulence intensity for the simulation of isothermal and nonisothermal subsonic round jet flow were in excellent conformance with other numerical simulations and available experimental data. This implies that the LES methodology works well with the compressible LBM framework for the simulation of subsonic turbulent flows. In particular, the very good agreement between the LBM-LES or KT-LBM-LES predictions and the experimental data

suggests that the proposed methodologies are relevant for addressing the accurate simulation of compressible subsonic turbulent flows.

In addition to the velocity field, it was shown how the LBM–LES (or, equivalently, the KT-LBM–LES) methodology can be used to predict the acoustics associated with a subsonic jet flow in both the near-field and far-field regimes. More specifically, the near-field properties (sound pressure levels and sound pressure spectrum levels) of the jet noise predicted using this methodology have been shown to be in good qualitative and quantitative agreement with well-known features of jet noise. Finally, it was shown how the Kirchhoff–Helmholtz integral methodology can be incorporated with an LBM–LES methodology for the prediction of the acoustic field of a subsonic turbulent jet in the far-field regime. With respect to the application of this methodology to an isothermal round jet flow, the directivity of the overall sound pressure level at a distance of $r_0 = 72D_j$ along the jet (x) axis for a range of elevation angles $\theta = 15^\circ$ to 90° was simulated and found to be in good agreement with some experimental data. Furthermore, the predicted sound pressure level spectra for an isothermal jet flow at various Mach numbers at various radial and axial distances from the jet nozzle and at various azimuthal angles from the jet axis in the both the near-field and far-field regimes of the acoustic field were found to be in very good conformance with some experimental data. These positive results suggest that the proposed methodology can be incorporated with more sophisticated compressible LBM models for the prediction of the hydrodynamical and aeroacoustic fields for computational aeroacoustic applications for both subsonic and (potentially) supersonic flows.

ACKNOWLEDGMENT

This work is funded by the Canadian Bureau for International Education (CBIE)-Libyan-North American Scholarship Program (LNASP).

ORCID

Khalid Noah  <https://orcid.org/0000-0002-5492-6891>

REFERENCES

1. Mattila K. *Implementation Techniques for the Lattice Boltzmann Method*. Finland: University of Jyväskylä; 2010.
2. Kruger T, Kusumaatmaja H, Kuzmin A, Shardt O, Silva G, Viggien EM. *The Lattice Boltzmann Method: Principles and Practice*. Switzerland: Springer International Publishing; 2017.
3. Bao YB, Meskas J. Lattice Boltzmann method for fluid simulations. Paper presented at: Proceedings of the 6th Annual IRMACS Day, Burnaby, British Columbia, Canada; 2011.
4. Feng W, He B, Song A, Wang Y, Zhang M, Zhang W. Compressible lattice Boltzmann method and applications. *Int J Numer Anal Model*. 2012;9:410–418.
5. Chen S. A large-eddy-based lattice Boltzmann model for turbulent flow simulation. *Appl Math Comput*. 2009;215:591–598.
6. Hou S, Sterling J, Chen S, Doolen G. A lattice Boltzmann subgrid model for high Reynolds number flows. *Fields Inst Commun*. 1994;6:151–166.
7. Jiang X, Lai C. *Numerical Techniques for Direct and Large-Eddy Simulations*. Boca Raton, FL: CRC Press; 2009.
8. Fernandino M, Beronov K, Ytrehus T. Large eddy simulation of turbulent open duct flow using a lattice Boltzmann approach. *Math Comput Simul*. 2009;79:1520–1526.
9. Dong Y, Sagaut P, Marie S. Inertial consistent subgrid model for large-eddy simulation based on the lattice Boltzmann method. *Phys Fluids*. 2008;20:035104–01–035104–12.
10. Dong Y-H, Sagaut P. A study of time correlations in lattice Boltzmann-based large-eddy simulation of isotropic turbulence. *Phys Fluids*. 2008;20(1–11):035105.
11. Si H, Shi Y. Study on lattice Boltzmann method/large eddy simulation and its application at high Reynolds number flow. *Adv Mech Eng*. 2015;7(3):1–8. <http://dx.doi.org/10.1177/1687814015573829>.
12. Cercignani C. *The Boltzmann Equation and Its Applications*. New York, NY: Springer; 1988.
13. Buick JM, Greated CA, Campbell DB. Lattice BGK simulation of sound waves. *Europhys Lett*. 1998;43:235–240.
14. Bhatnagar P, Gross P, Krook M. A model for collision processes in gases. I. small amplitude processes in charged and neutral one-component systems. *Phys Rev*. 1954;94:511–525.
15. Lew P, Mongeau L, Lyrintzis A. Noise prediction of a subsonic turbulent round jet using the lattice-Boltzmann method. *J Acoust Soc Am*. 2010;128(11–18):1118–1127.
16. Yu H, Girimaji SS. Near-field turbulent simulations of rectangular jets using lattice Boltzmann method. *Phys Fluids*. 2005;17(1–17):125106.
17. Yang Y, Chang S, Chiou C. Lattice Boltzmann method and large-eddy simulation for turbulent impinging jet cooling. *Int J Heat Mass Transf*. 2013;61:543–553.
18. Shouxin H, Guangwu Y, Weiping H. A lattice Boltzmann model for compressible perfect gas. *Acta Mech Sinica*. 1997;13:218–226.
19. Shan X, He X. Discretization of the velocity space in the solution of the Boltzmann equation. *Phys Rev Lett*. 1998;80:65–68.

20. Yan G, Chen Y, Hu S. Simple lattice Boltzmann model for simulating flows with shock wave. *Phys Rev E*. 1999;59:454-459.
21. Kataoka T, Tsutahara M. Lattice Boltzmann method for the compressible Euler equations. *Phys Rev*. 2004;69:056702-1-056702-14.
22. Kataoka T, Tsutahara M. Lattice Boltzmann model for the compressible Navier-Stokes equations with flexible specific-heat ratio. *Phys Rev*. 2004;69:035701-1-035701-4.
23. Qu K, Shu C, Chew Y. Alternative method to construct equilibrium distribution functions in lattice-Boltzmann method simulation of inviscid compressible flows at high mach number. *Phys Rev E*. 2007;75:036706-1-036706-13.
24. Wang Y, He YL, Zhao TS, Tang GH, Tao WQ. Implicit-explicit finite-difference lattice Boltzmann method for compressible flow. *Int J Modern Phys C*. 2007;18:1961-1983.
25. Li Q, He YL, Wang Y, Tao WQ. Coupled double-distribution-function lattice Boltzmann method for the compressible Navier-Stokes equations. *Phys Rev E*. 2007;76:056705.
26. Li Q, He YL, Wang Y, Tang GH. Three-dimensional non-free-parameter lattice Boltzmann model and its application to inviscid compressible flows. *Phys Lett A*. 2009;373:2101-2108.
27. Wang Y, He YL, Li Q, Tang GH, Tao WQ. Lattice Boltzmann model for simulating viscous compressible flow. 2010;21:383-407.
28. Smagorinsky J. General circulation experiments with the primitive equations. *Meteorol Z*. 1963;91:99-164.
29. Guo Z, Shu C. *Lattice Boltzmann Method and its Applications in Engineering*. Singapore, Asia: World Scientific; 2013.
30. Li Q, Zhong C, Li K, et al. Implementation of a lattice Boltzmann method for large eddy simulation on multiple GPUs. Paper presented at: Proceedings of the IEEE 14th International Conference on High Performance Computing and Communication and 2012 IEEE 9th International Conference on Embedded Software and Systems, Washington, DC; 2012.
31. Bridges J, Wernet M. Measurements of the aeroacoustic sound source in hot jets. Paper presented at: Proceedings of the 9th AIAA/CEAS Aeroacoustics Conference and Exhibit, South Carolina; 2003.
32. Laurendeau E, Bonnet JP, Jordan P, Delville J. Impact of fluidic chevrons on the turbulence structure of a subsonic jet. Paper presented at: Proceedings of the 3rd AIAA Flow Control Conference; 2006; San Francisco.
33. Chen S, Martinez D, Mei R. On boundary conditions in lattice Boltzmann method. *Phys Fluids*. 1996;8:2527-2536.
34. Rajaratnam N, Khan AA. Intersecting circular turbulent jets. *J Hydraul Res*. 1992;30:373-387.
35. Morfey C, Szewczyk V, Tester B. New scaling laws for hot and cold jet mixing noise based on a geometric acoustics model. *J Sound Vib*. 1978;61:255-292.
36. Mancinelli M, Pagliaroli T, Marco AD, Camussi R, Castelain T. Wavelet decomposition of hydrodynamic and acoustic pressures in the near field of the jet. *J Fluid Mech*. 2017;813:716-749.
37. Marburg S, Nolte B. *Computational Acoustics of Noise Propagation in Fluids: Finite and Boundary Element Methods*. Berlin, Germany: Springer; 2008.
38. Lyrantzis A, Mankbadi R. On the prediction of the far-field jet noise using Kirchhoff's formulation. *AIAA J*. 1996;34:413-416.
39. Pan FL, Uzun A, Lyrantzis AS. Surface integral methods in jet aeroacoustics: refraction corrections. *J Aircr*. 2008;45:381-387.
40. Tanna H. An experimental study of jet noise Part I: turbulent mixing noise. *J Sound Vib*. 1977;50:405-428.
41. Lighthill MJ. On sound generated aerodynamically I. general theory. *Proc Royal Soc A Math Phys Eng Sci*. 1952;211:564-587.
42. Kumar R, Krothapalli A, Greska B. Near-field noise characteristics of a pulse jet. Paper presented at: Proceedings of the 14th AIAA/CEAS Aeroacoustics Conference and 29th AIAA Aeroacoustics Conference, Vancouver, British Columbia, Canada; May 2008.
43. Barre S, Fleury V, Bogey C, Bailly C, and Juve D. Experimental study of the properties of near-field and far-field jet noise. Paper presented at: 12th AIAA/CEAS Aeroacoustics Conference and 27th AIAA Aeroacoustics Conference; 2006; Ecully, France.

How to cite this article: Noah K, Lien F-S, Yee E. Large-eddy simulation of subsonic turbulent jets using the compressible lattice Boltzmann method. *Int J Numer Meth Fluids*. 2021;93:927-952. <https://doi.org/10.1002/fld.4914>